

Highlights

Microbubble surface instabilities in a strain stiffening viscoelastic material

Sawyer Remillard, Bachir A. Abeid, Timothy L. Hall, Jonathan R. Sukovich, Jacob Baker, Jin Yang, Jonathan B. Estrada, Mauro Rodriguez Jr.

- Kinematically-consistent bubble surface perturbation evolution model for strain stiffening viscoelastic materials
- Theoretical model validation for the evolution of bubble surface perturbations in viscoelastic materials
- Tunable strain-rate material characterization from a single experimental setup

Microbubble surface instabilities in a strain stiffening viscoelastic material

Sawyer Remillard^{a,*}, Bachir A. Abeid^b, Timothy L. Hall^c, Jonathan R. Sukovich^c, Jacob Baker^d, Jin Yang^{e,f}, Jonathan B. Estrada^b and Mauro Rodriguez Jr.^{a,**}

^a*School of Engineering, Brown University, Providence, 02912, RI, USA*

^b*Department of Mechanical Engineering, University of Michigan, Ann Arbor, 48109, MI, USA*

^c*Department of Biomedical Engineering, University of Michigan, Ann Arbor, 48109, MI, USA*

^d*Department of Biomedical Engineering, The University of Texas at Austin, Austin, 78712, TX, USA*

^e*Department of Aerospace Engineering and Engineering Mechanics, The University of Texas at Austin, Austin, 78712, TX, USA*

^f*Texas Materials Institute, The University of Texas at Austin, Austin, 78712, TX, USA*

ARTICLE INFO

Keywords:

Inertial cavitation
Material characterization
Nonspherical bubble dynamics
Strain hardening
Viscoelasticity

ABSTRACT

Understanding the dynamics of instabilities along fluid-solid interfaces is critical for the efficacy of focused ultrasound therapy tools (e.g., histotripsy) and microcavitation rheometry techniques. Non-uniform pressure fields generated by either ultrasound or a focused laser can cause non-spherical microcavitation bubbles. Previous perturbation amplitude evolution models in viscoelastic materials either assume pure radial deformation or have inconsistent kinematic fields between the fluid and solid contributions. We derive a kinematically-consistent theoretical model for the evolution of surface perturbations. The model captures the non-linear kinematics of a strain-stiffening viscoelastic material surrounding a non-spherical bubble. The model is validated for (i) small, approximately linear radial oscillations and (ii) large inertial oscillations using laser-induced microcavitation experiments in a soft hydrogel. For the former, the bubble is allowed to reach mechanical equilibrium, and then surface perturbations are excited using ultrasound forcing. For the latter, the microbubble forms small bubble surface perturbations at its maximum radius that grow during collapse. The model's dominant surface perturbation mode scales linearly with equilibrium radius and matches experiments. Similarly, the model's perturbation amplitude evolution sufficiently constrains the rheometry problem and is experimentally validated.

1. Introduction

Experiments and simulations show that cavitation bubbles rarely stay perfectly spherical during their oscillations, especially in soft viscoelastic materials [15, 6, 12, 20, 29, 24, 25, 43, 42, 41]. Asphericities form during applications of cavitation in soft materials such as histotripsy [38, 22, 23, 39, 3] and Inertial Microcavitation Rheometry (IMR) [30, 8, 40] which can decrease their efficacy. In contrast, the non-spherical oscillations increase the efficacy of targeted drug release [19, 36, 16]. However, modeling this phenomenon is limited to two models across three studies [43, 9, 24] where each model uses different assumptions, leading to disagreement.

Although the study of non-spherical cavity oscillations in viscoelastic solid materials is quite recent, it has been a topic studied extensively in fluids, dating back to Plesset [28]. Prosperetti [30] included viscosity and vorticity effects. The latter led to a computationally expensive model, which must be solved directly rather than analytically linearized for a stability analysis. To simplify Prosperetti's model, Hilgenfeldt et al. [14] restricted the vorticity modeling to a viscous boundary layer. This model agreed with experimental data

by Versluis et al. [37]. Later models include higher-order terms in the perturbation series expansion to compute energy transfer between the volumetric and the shape mode oscillations [13, 33, 35, 34]. Variants of the model from Shaw [33] agreed with the following two experimental studies. Guédra et al. [11] showed the coupling between the perturbation modes and radial dynamics, where ultrasound forcing was used over prolonged periods of time to excite these non-spherical modes. In the work by Cleve et al. [7], nonspherical oscillations were first induced through bubble coalescence, then forced via ultrasound transducers. However, these models are only valid for Newtonian fluids, a special case of a material model whose viscous Cauchy stress is proportional to the applied strain rate.

Non-spherical cavity modeling has been extended to elastic solid materials. Gaudron et al. [9] developed a model of non-spherical bubble oscillations and considered both neo-Hookean hyperelastic and linear elastic material models. The model was extended by Murakami et al. [24] to include vorticity and viscosity and was shown to agree with part of the experimental data from Hamaguchi and Ando [12] as well as Saint-Michel and Garbin [32]. However, the models of Murakami et al. [24] and Gaudron et al. [9] utilized inconsistent kinematic fields for acceleration and material deformation. The velocity potential approach from Plesset [28] was used for the former, while for the latter, when computing the elastic contribution to the divergence of the Cauchy Stress, pure radial deformation was assumed.

*Corresponding author

**Principal corresponding author

ORCID(S): 0000-0002-5469-6168 (S. Remillard); 0009-0009-0859-8434 (B.A. Abeid); 0000-0002-4867-2856 (T.L. Hall); 0000-0002-5650-991X (J.R. Sukovich); 0000-0003-3361-1513 (J. Baker); 0000-0002-5967-980X (J. Yang); 0000-0003-1083-4597 (J.B. Estrada); 0000-0003-0545-0265 (M.R. Jr.)

Using two different kinematic fields on the same material is physically unrealistic. The approach leads to incorrect predictions when the shear modulus becomes large or if the material experiences large stretch ratios. Separately, Yang et al. [43] developed a nonspherical model for visco-hyperelastic materials which show strain stiffening. They show agreement with experiments for the model's prediction of the instability growth and decay through an eigenvalue analysis of the model governing equations. The model uses consistent kinematic fields throughout the derivation, however, only considers radial motion and neglects angular deformations. To date, the non-spherical models of [43, 9, 24] which account for viscoelasticity have not been validated with perturbation evolution data from experiments.

We hypothesize that angular deformation is necessary for comparing direct observations of the perturbation mode and amplitude evolution to the theory as it was considered for fluid validated models. Moreover, non-spherical oscillations can be used to characterize viscoelastic materials across a range of strain rates. For an ultrasound forced system, the strain rate experienced by the material is tunable by the forcing frequency and bubble size. To that end, the objective of this work is to: (i) develop and validate a kinematically consistent, spherical surface perturbation model that includes angular deformations and (ii) use perturbation dynamics to constrain material characterization techniques. The proposed model is presented in section 2. Small radial oscillations model simplifications are presented in section 3. The model is compared with existing models in section 4. The numerical and experimental methods are described in section 5. The results and discussion comparing theory and experiments are presented in section 6. We conclude with our contributions in section 7.

2. Kinematically consistent analytical model

2.1. Geometry

Figure 1 shows the problem set-up and an example of a uniform grid transformation from the reference configuration from axisymmetric spherical harmonic modes. A spherical bubble is in stress-free mechanical equilibrium with the surrounding material and reference radius R_o . The bubble surface is

$$\mathcal{R}(t, \theta, \phi) = R(t) \left(1 + \sum_{n,m} \epsilon_n(t) Y_n^m \right),$$

where R is the mean bubble radius, ϵ_n the non-dimensional amplitude of the surface perturbation, t time, and $Y_n^m = Y_n^m(\theta, \phi)$ the real spherical harmonics with mode number n and azimuthal order m in the current coordinates. Perturbation amplitude and bubble radius time dependency and summation of the modes are dropped for brevity.

The reference spherical coordinate system is $\psi_o = (r_o, \theta_o, \phi_o)$ and the current $\psi = (r, \theta, \phi)$. The position vectors in the reference and current coordinates are,

$$\mathbf{x}_o = r_o \hat{\mathbf{e}}_r(\theta_o, \phi_o), \quad \mathbf{x} = r \hat{\mathbf{e}}_r(\theta, \phi), \quad (1)$$

where $\hat{\mathbf{e}}_r$ is the radial direction unit vector. The current position vector is decomposed into the base radial deformation with superposed first order small non-spherical deformation,

$$\mathbf{x} = r_s \hat{\mathbf{e}}_r(\theta_o, \phi_o) + \epsilon_n \mathbf{u}_1, \quad (2)$$

where r_s is the base spherical deformation, and \mathbf{u}_1 the nonspherical surface perturbation deformation vector. Since the non-spherical motion is assumed to be small relative to the spherical motion, i.e., $\epsilon_n(t) \ll 1$, then terms $\mathcal{O}(\epsilon_n^2)$ and higher are truncated. Then, the motion map from the reference to current coordinates is denoted as χ :

$$\psi = \chi(\psi_o) = \chi_s(\psi_o) + \epsilon_n \chi_1(\psi_o),$$

where,

$$\begin{aligned} \chi_s(\psi_o) &= (r_s(r_o, t), \theta_o, \phi_o), \\ \chi_1(\psi_o) &= (r_1(\psi_o, t), \theta_1(\psi_o, t), \phi_1(\psi_o, t)). \end{aligned}$$

Here, χ_1 , r_1 , θ_1 , and ϕ_1 are the respective first-order terms to the total coordinate, radial, θ , and ϕ maps. Plugging the coordinate deformation map into equations (1) and (2) and linearizing we obtain

$$\mathbf{u}_1 = r_1 \hat{\mathbf{e}}_r + r_s \theta_1 \hat{\mathbf{e}}_\theta + r_s \sin \theta_o \phi_1 \hat{\mathbf{e}}_\phi, \quad (3)$$

where $\hat{\mathbf{e}}_\theta$ and $\hat{\mathbf{e}}_\phi$ are unit vectors in the polar and azimuthal direction, respectively. The unit vectors in equation (3) are functions of θ_o and ϕ_o only. Since $(\theta, \phi) = (\theta_o, \phi_o) + \mathcal{O}(\epsilon_n)$, then when computing the position vector, the components of \mathbf{u}_1 can be written in either coordinate basis to first order accuracy.

2.2. Kinematics

The deformation gradient tensor is

$$\mathbf{F} = \frac{\partial \mathbf{x}}{\partial \mathbf{x}_o} = \begin{bmatrix} \frac{\partial r}{\partial r_o} & \frac{1}{r_o} \frac{\partial r}{\partial \theta_o} & \frac{1}{r_o \sin \theta_o} \frac{\partial r}{\partial \phi_o} \\ r \frac{\partial \theta}{\partial r_o} & \frac{r}{r_o} \frac{\partial \theta}{\partial \theta_o} & \frac{r_o \sin \theta_o}{r} \frac{\partial \theta}{\partial \phi_o} \\ r \sin \theta \frac{\partial \phi}{\partial r_o} & \frac{r \sin \theta}{r_o} \frac{\partial \phi}{\partial \theta_o} & \frac{r \sin \theta}{r_o \sin \theta_o} \frac{\partial \phi}{\partial \phi_o} \end{bmatrix}, \quad (4)$$

and written in the expanded coordinate maps in [31]. The deformation gradient can be decomposed as a sum of powers of ϵ_n , $\mathbf{F} = \mathbf{F}_s + \epsilon_n \mathbf{F}_1$. Material incompressibility is satisfied with $\det(\mathbf{F}) = 1$. After truncating terms of $\mathcal{O}(\epsilon_n^2)$ and higher, the incompressibility condition becomes

$$\det(\mathbf{F}) \approx \det(\mathbf{F}_s) + \epsilon_n \left[\frac{\partial}{\partial \epsilon_n} \det(\mathbf{F}) \right]_{\epsilon_n=0} = 1.$$

By the method of perturbation matching and consistent with Ogden and Sinclair [27], $\det(\mathbf{F}_s) = 1$ and the incremental deformation incompressibility condition is

$$\left[\frac{\partial}{\partial \epsilon_n} \det(\mathbf{F}) \right]_{\epsilon_n=0} = \text{tr}(\mathbf{F}_s^{-1} \mathbf{F}_1) = \nabla_{\mathbf{x}} \cdot \mathbf{u}_1 = 0. \quad (5)$$

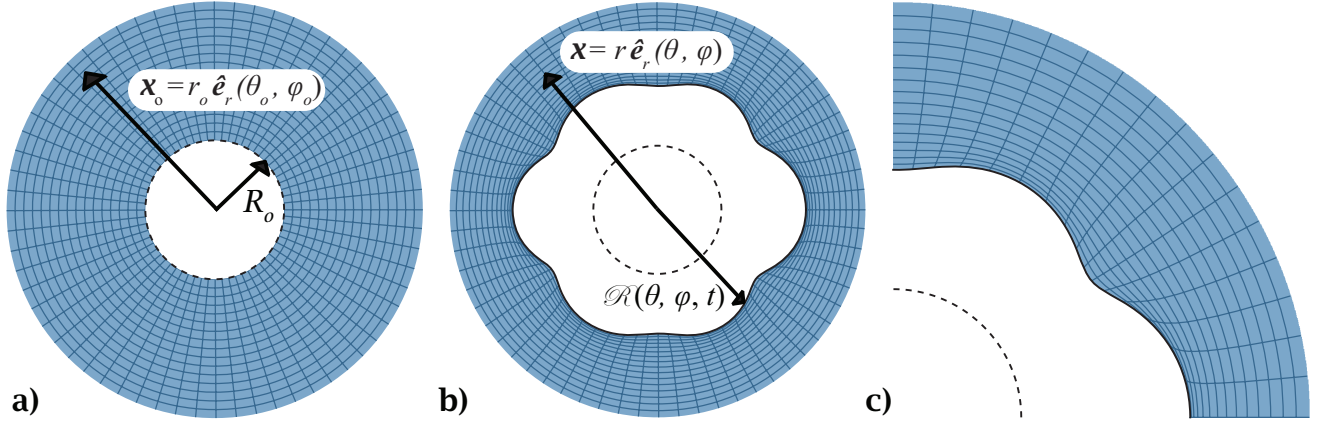


Figure 1: Problem set-up shown as a cross-section for constant ϕ . **a)** Reference configuration with the bubble at the mechanical equilibrium radius shown in dashed lines. **b)** An example current configuration with base radial growth and formation of the spherical harmonic instabilities. **c)** Zoom in of material grid and bubble distortion of the top right quadrant of b).

The base state deformation for the purely spherical case is well known as [8, 10, 43]. The incompressibility relationship for the base deformation is

$$r_s = (r_o^3 + R^3 - R_o^3)^{1/3}. \quad (6)$$

Equation (5) is solved for the mappings proportional to ϵ_n . We consider the following ansatz for the displacement,

$$\mathbf{u}_1 = \nabla_{\mathbf{x}} [f(r) Y_n^m], \quad (7)$$

where $f(r)$ is a function of the spatial radial coordinate. The rotational part of the perturbed displacement field which would form due to the presence of interfacial perturbations, viscosity, and elasticity is not considered for simplicity.

Substituting equation (7) into the spatial divergence of the perturbed displacement field, linearizing, and using the characteristic equation of the spherical harmonics, the incompressibility condition simplifies to an ordinary differential equation

$$r^2 f'' + 2r f' - n(n+1)f = 0. \quad (8)$$

The corresponding decaying solution of the above equation is $f = C_1 r^{-n-1}$, where C_1 is solved for via the radial displacement boundary condition on the bubble surface:

$$r(r_o = R_o, \theta_o, \phi_o, t) = R(1 + \epsilon_n Y_n^m) \rightarrow f'|_{r=R} Y_n^m = R Y_n^m,$$

with $C_1 = -R^{n+3}/(n+1)$. Then, the respective velocity and acceleration are calculated via,

$$\mathbf{v} = \dot{r} \hat{\mathbf{e}}_r + r\dot{\theta} \hat{\mathbf{e}}_\theta + r \sin \theta \dot{\phi} \hat{\mathbf{e}}_\phi, \quad (9a)$$

$$\begin{aligned} \mathbf{a} = & (\ddot{r} - r\dot{\theta}^2 - r\dot{\phi}^2 \sin^2 \theta) \hat{\mathbf{e}}_r \\ & + (r\ddot{\theta} + 2r\dot{\theta}\dot{\phi} - r\dot{\phi}^2 \sin \theta \cos \theta) \hat{\mathbf{e}}_\theta \\ & + (r\ddot{\phi} \sin \theta + 2r\dot{\theta}\dot{\phi} \sin \theta + 2r\dot{\theta}\dot{\phi} \cos \theta) \hat{\mathbf{e}}_\phi, \end{aligned} \quad (9b)$$

where dot operators are time derivatives at constant reference coordinates and the unit vectors are with respect to the current coordinate basis. The coordinate deformation map, linearized inverse coordinate deformation map, and Eulerian velocities and accelerations are listed in [31].

2.3. Momentum balance

Momentum balance equation is

$$\rho \mathbf{a} = \nabla_{\mathbf{x}} \cdot \boldsymbol{\sigma}, \quad (10)$$

where ρ is the material density and $\boldsymbol{\sigma}$ the Cauchy stress tensor. Considering the quadratic Kelvin-Voigt (qKV) constitutive model [18, 40],

$$\boldsymbol{\sigma} = G (1 + \alpha(I_B - 3)) \mathbf{B} + 2\mu \mathbf{D} - \mathcal{P} \mathbf{I}, \quad (11)$$

where G is the shear modulus, α the strain stiffening parameter, μ the viscosity, and \mathbf{I} the identity tensor. I_B is the first invariant of \mathbf{B} , linearized with respect to the perturbation amplitude, i.e.,

$$\begin{aligned} I_B = & \frac{2r^6 + \varrho^2}{r^4 \varrho^{2/3}} + \frac{2\epsilon_n R^{n+3}}{r^{n+7} \varrho^{5/3}} (R^3 - R_o^3) (2r^3 - R^3 + R_o^3) \\ & \times ((n+2)r^3 + n(R_o^3 - R^3)) Y_n^m, \end{aligned} \quad (12)$$

where $\varrho = (r^3 - R^3 + R_o^3)^{1/3}$. $\mathbf{B} = \mathbf{F} \mathbf{F}^\top$ is the left Cauchy-Green deformation tensor and not deviatoric, thus \mathcal{P} is a pressure-like quantity and related to the hydrostatic pressure. \mathbf{D} is the rate of strain tensor, i.e.,

$$\mathbf{D} = \frac{1}{2} (\nabla_{\mathbf{x}} \mathbf{v} + (\nabla_{\mathbf{x}} \mathbf{v})^\top).$$

The components of the \mathbf{B} and \mathbf{D} tensors used in equation (11) are listed in [31]. Additionally,

$$\mathcal{P} = \mathcal{P}_s + \epsilon_n \mathcal{P}_1 Y_n^m,$$

where \mathcal{P}_s and \mathcal{P}_1 are the respective base state pressure and surface perturbations contributions.

2.4. Boundary conditions

The two boundary conditions of the system are (i) traction at the bubble wall and (ii) stress-free in the far field.

The inertia and viscosity of the gas or vapor is negligible compared to that of the surrounding fluid [5, 24]. After linearization, the radial-normal component of the traction and far field boundary condition are

$$\sigma_{rr}|_{r=R(1+\epsilon_n Y_n^m)} = -p_b + \frac{2\gamma}{R} + \frac{(n+2)(n-1)\gamma}{R} \epsilon_n Y_n^m, \quad (13a)$$

$$\sigma_{rr}|_{r \rightarrow \infty} = -p_\infty, \quad (13b)$$

respectively, where γ is the surface tension between the two phases, p_b the bubble internal pressure, p_∞ the far-field pressure. Similar to [10, 24, 43], we lack the degrees of freedom in our ansatz to enforce tangential stress continuity.

2.5. Equations of motion

Integrating the radial component of equation (10), applying spherical orthogonality (multiplying by $\sin(\theta)Y_0^0$ and integrating in θ and ϕ), and applying the two stress boundary conditions yields the Rayleigh-Plesset equation,

$$R\ddot{R} + \frac{3}{2}\dot{R}^2 = \frac{1}{\rho_m} \left(p_b - p_\infty - \frac{2\gamma}{R} + S \right). \quad (14)$$

The stress integral for a qKV model is

$$S = \frac{(3\alpha - 1)G}{2} [5 - \lambda^{-4} - 4\lambda^{-1}] + 2\alpha G \left[\frac{27}{40} + \frac{1}{8}\lambda^{-8} + \frac{1}{5}\lambda^{-5} + \lambda^{-2} - 2\lambda \right] - \frac{4\mu\dot{R}}{R}, \quad (15)$$

where λ is the spherical stretch ratio of the material at the bubble wall $\lambda = R/R_o$. Multiplying equation (10) by $\sin(\theta)Y_n^m$ and applying orthogonality yields:

$$\ddot{\epsilon}_n + \eta\dot{\epsilon}_n + \xi\epsilon_n = 0, \quad (16)$$

where coefficients η and ξ for the current model and models of Yang et al. [43] and Murakami et al. [24] without the rotational corrections are in [31]. Since $\mathcal{O}(\epsilon_n^2)$ and higher terms are neglected, modes are decoupled and depend only on radial motion. Here, we only consider the irrotational models of Murakami et al. [24] and Prosperetti [30].

3. Linearized stability analysis

Predicting the initial condition to the growth of the surface perturbations under ultrasonic forcing is challenging in experiments because it often begins as a seed of the order of $\mathcal{O}(10^{-3})$ [24]. Upon termination of the ultrasonic forcing, the perturbation amplitudes decay to equilibrium. The initial condition for the decay process is simpler since the perturbation amplitudes will be of finite amplitude. Considering small radial oscillations due to ultrasonic forcing, the bubble radius evolution can be approximated as $R(t) = R_o(1 + \Delta\lambda(t))$ where $\Delta\lambda(t) = \lambda(t) - 1 = \mathcal{O}(\epsilon_n)$. The pressure surrounding the bubble is $p_\infty = p_{\text{atm}} + \mathcal{A} \cos(2\pi f t)$, where \mathcal{A} is the amplitude of the forcing and f the frequency.

Linearizing equation (16) about small radial oscillations, the coefficients are

$$\eta_l = \frac{2(n+2)(n+1)\mu}{\rho R_o^2}, \quad (17a)$$

$$\xi_l = \omega_n^2 = \frac{2(n+2)(n+1)}{\rho R_o^2} \left(G + \frac{(n-1)\gamma}{2R_o} \right), \quad (17b)$$

where the subscript 1 denotes linearized quantities and ω_n is the surface perturbation mode natural frequency.

The prediction of the most unstable (dominant) mode for given material properties, ultrasound forcing, and equilibrium bubble radius satisfy the parametric resonance condition, $2\omega_n/\omega_0 = 1$, where $\omega_0 = 2\pi f$ is the angular forcing frequency. This 1:2 resonance condition is from Mathieu's equation theory [21] and was verified experimentally for non-spherical bubbles [37].

Prescribing an initial finite amplitude, $\epsilon_{n,0} = \epsilon_n(t=0)$, and $\dot{\epsilon}_n(t=0) = 0$, there is an analytical solution for the perturbation equation for linearized radial motion:

$$\epsilon_n(t) = \epsilon_{n,0} \exp\left(-\frac{t\eta_l}{2}\right) \left[\cosh\left(\frac{t\delta_l}{2}\right) + \frac{\eta_l}{\delta_l} \sinh\left(\frac{t\delta_l}{2}\right) \right], \quad (18)$$

$$\text{where } \delta_l = \sqrt{\eta_l^2 - 4\xi_l}.$$

4. Comparison of analytical models

Table 1 tabulates the differences between the models of [30], [24], [43], and the present model. For zero shear modulus, the models from Murakami et al. [24] and Prosperetti [30] are equivalent. However, the model from Yang et al. [43] and the present model do not simplify in this way for zero shear modulus. Only in the limit of linearized radial oscillations and zero shear modulus, the current model and the model from Prosperetti [30] are equivalent, this is explained through vorticity. The present perturbed displacement field is curl-free but does not guarantee a curl-free velocity or acceleration field. Taking the Eulerian curl of the velocity described in equation (9a), we obtain:

$$\nabla_{\mathbf{x}} \times \mathbf{v} = 6\epsilon_n \frac{n+2}{n+1} \frac{R^{5+n}\dot{R}}{r^{6+n}} \left(\frac{1}{\sin\theta} \frac{\partial Y_n^m}{\partial\phi} \hat{\mathbf{e}}_\theta - \frac{\partial Y_n^m}{\partial\theta} \hat{\mathbf{e}}_\phi \right). \quad (19)$$

If the radial motion is linear or static, there is no vorticity and the irrotational model assumptions are valid [30]. However, as is seen in [31], this vorticity residual leads to a vorticity equation that we cannot directly enforce. This is a persistent issue across the models of Yang et al. [43] and Murakami et al. [24] contributing to causing violation of the θ and ϕ components of the momentum balance. To satisfy the three momentum balance equations, more degrees of freedom are needed in the ansatz for the displacement field. However, it

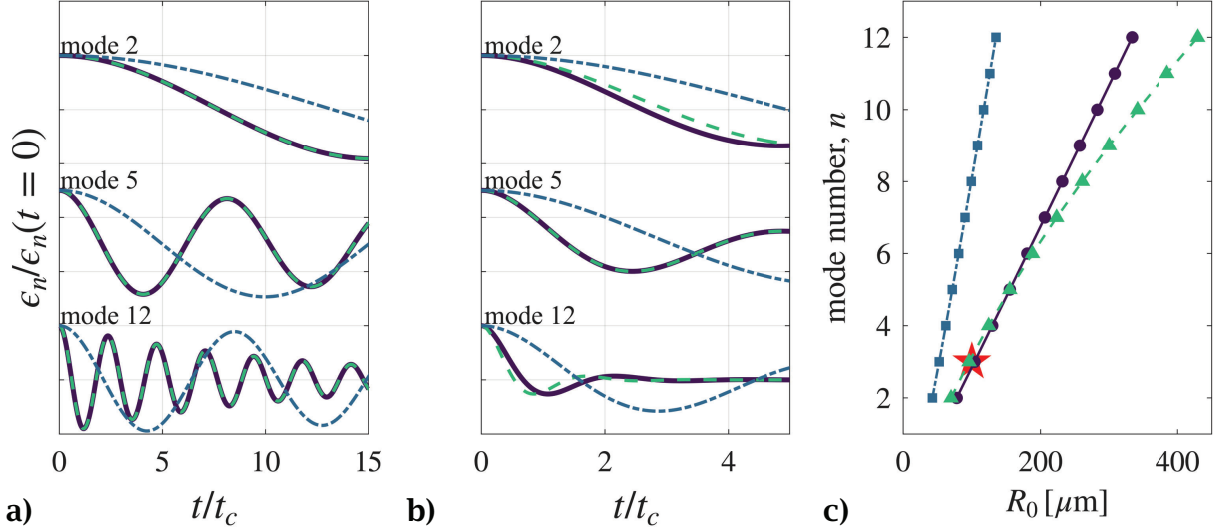


Figure 2: Perturbation evolution under linear radial motion for **a)** fluid **b)** a viscoelastic solid and **c)** most unstable mode prediction. Dashed green lines: Murakami et al. [24]; dashed-dotted light blue lines: Yang et al. [43]; and solid dark blue lines: current theory.

is shown by Prosperetti [30] that the dominant effect to the perturbation amplitude evolution (for viscous fluids), is due to the contribution from the gradient based ansatz.

Given linear radial motion and a zero-shear modulus, the coefficients, ξ_l and η_l from Prosperetti [30], Murakami et al. [24], and the present work agree (see [31]). Comparing ξ_l and η_l from Yang et al. [43], Murakami et al. [25], and equation (17b) and equation (17a), the coefficients of μ and G are equivalent when the kinematic fields are consistent. When kinematic fields are consistent, the leading order power of the equilibrium radius, R_o matches the inverse of the leading order power of the mode number n in ξ_l which leads to a linear scaling of the most unstable mode as a function of R_o . To show the equivalency between models, we consider a $200\text{ }\mu\text{m}$ bubble in water ($\mu = 1\text{ mPa}\cdot\text{s}$ and $\gamma = 72\text{ mN/m}$) with static radial motion. We initialize modes 2, 5, and 12 out of equilibrium at an initial amplitude of 0.1. Figure 2 a) shows the current model exactly matches the model by Prosperetti [30], here $t_c = R_{\max}\sqrt{\rho/p_\infty}$. The disagreement between the Yang et al. [43] and present model is due to the missing factor of $\sqrt{n+1}$ in the perturbation mode natural frequency due to angular motion. Inclusion of angular motion changes the solution of the displacement field obtained from the incompressibility condition to localize more material strain to the bubble surface, explaining the increased frequency.

With the same initial conditions we simulate a soft material with material properties calibrated in Hamaguchi and Ando [12], $G = 1.7\text{ kPa}$, $\mu = 14.1\text{ mPa}\cdot\text{s}$, and $\gamma = 40\text{ mN/m}$. The results are shown in figure 2 b). The model from [24] under and overestimates the frequency of oscillation and for low and high mode numbers, respectively. The frequency discrepancy between the present model and the model by Murakami et al. [24] is explained by the scaling of ξ_l with respect to the equilibrium radius and

Table 1
Comparison of linearized bubble surface perturbation models.

Analysis	Angular Motion	Finite elastic	Kinematic consistency
Prosperetti [30]	✓	✗	✓
Murakami et al. [24]	Hybrid	✓	✗
Yang et al. [43]	✗	✓	✓
Present work	✓	✓	✓

the mode number. Figure 2 c) shows the non-linear scaling between mode number and equilibrium radius predicted by Murakami et al. [24]. For $f = 28\text{ kHz}$, and $R_o \approx 100\text{ }\mu\text{m}$, three is the most unstable mode observed by [12]. We observe that the Murakami et al. [24] and the present models correctly predict the third mode as the most unstable. As equilibrium radii and therefore mode number increases, the difference between ξ_l from Murakami et al. [24] and the present model diverges.

5. Methods

5.1. Experiments

Figure 3 shows the experimental setup and follows our previously published work [2]. The set-up applies to both experiments: (i) laser-induced inertial cavitation (LIC) then ultrasound forced and (ii) LIC with large amplitude radial oscillations. For the latter experiments, an ultrasound transducer was not used. Images are processed using an edge detection-based MATLAB (MathWorks, MA, USA) processing routine. A single 4 ns pulse of a user-adjustable, frequency-doubled Q-switched 532 nm Nd:YAG laser (Continuum Minilite II, San Jose, CA) beam was aligned into a 10X/0.25 NA high-power microspot focusing objective (LMH-10X-532; Thorlabs, Newton, NJ). The laser beam

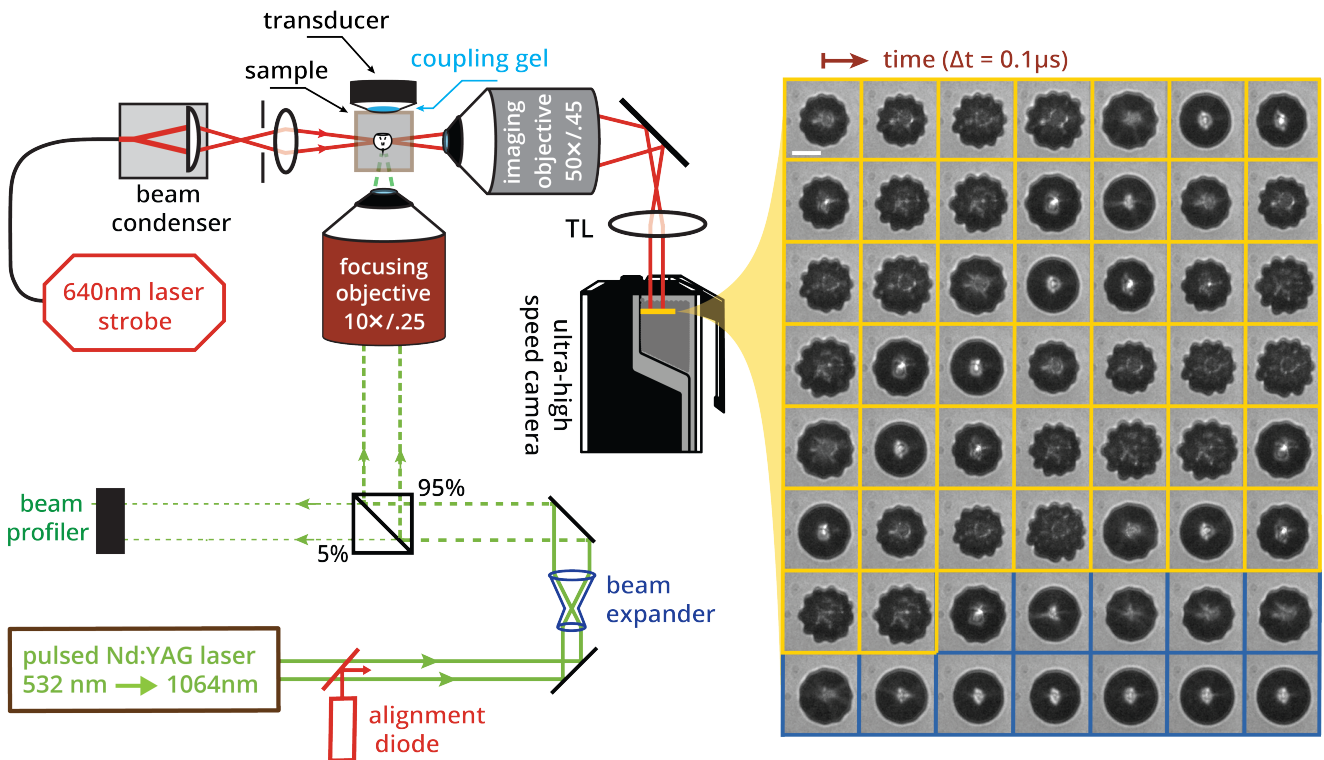


Figure 3: Experimental setup (drawn simplified) generates micro-cavitation using high energy laser, excites surface oscillations via in-house fabricated 10 mm diameter transducer, and records dynamics at 10^7 frames per second, 1 ms post cavitation. The maize-outlined frames show when the driving 750 kHz ultrasound was active, while frames outlined in blue show inactive ultrasound. Scale bar: 20 μm .

was directed using three broadband dielectric mirrors (BB1-E02; Thorlabs) and three short-pass dichroic mirrors. For alignment purposes, a dichroic mirror (DMSP605; Thorlabs) was aligned with a collimated continuous-wave laser diode (CPS635R; Thorlabs) to the pulsed beam to provide visible guidance. Prior to reaching the focusing objective, the collimated beam was expanded using a 2X fixed magnification beam expander (GBE02-A; Thorlabs) to match the back aperture of the objective and reduce the risk of optical damage. Infrared wavelengths were removed by a second dichroic mirror (HBSY052; Thorlabs), which redirected unwanted spectral components into a beam dump (LB2; Thorlabs).

For the ultrasound forced experiments, 1 ms after cavitation was induced, small radial oscillations were achieved via an XY translation-stage-mounted, 10 mm diameter cylindrical acoustic transducer. The ultrasonic forcing excited the previously generated bubble surface oscillations with a 50 cycle sinusoidal wave at 750 kHz and 720 kPa. An ultra-high-speed imaging camera (HPV-X2; Shimadzu, Kyoto, Japan) captured the bubble oscillations event at 10^7 frames per second.

The LIC experiments with nonspherical bubbles are part of a larger dataset of previously published data in Yang et al. [40]. Additional details on experimental setup differences and gel preparation are in [40, 31].

5.2. Data processing

A spectral interpolation approach is used to extract the perturbation amplitudes from the data points along the bubble surface [31]. A global search method (bayesopt) hybridized with a local search method (lsqcurvefit) in MATLAB is used to optimize the present model to the experimental data about the material properties μ , G , and α . For small radial oscillations, there is no effect on the dynamics from the strain stiffening parameter α and is therefore omitted from the optimization. The surface tension is set to 32 mN/m [17] and 56 mN/m [43] for the gelatin gels and polyacrylamide, respectively.

6. Results and discussion

6.1. Small amplitude radial oscillations

Figure 4 shows a) the data and model predictions, b) and c) extracted parameters, and d) the most unstable mode as a function of equilibrium radius for the 10% gelatin gel. 5% gelatin gel results are in [31]. Calibrated values for both viscosity and elasticity for each experiment are listed in [31]. The mean values of the shear moduli calibrated to equation (18) are $\bar{G}_{5\%} = 2.61$ kPa and $\bar{G}_{10\%} = 7.81$ kPa for the 5% and 10% gelatin gels respectively. Figure 5 summarizes shear modulus across selected studies with various gelatin gel compositions. The mean calibrated shear modulus and its scaling with composition is consistent between this study

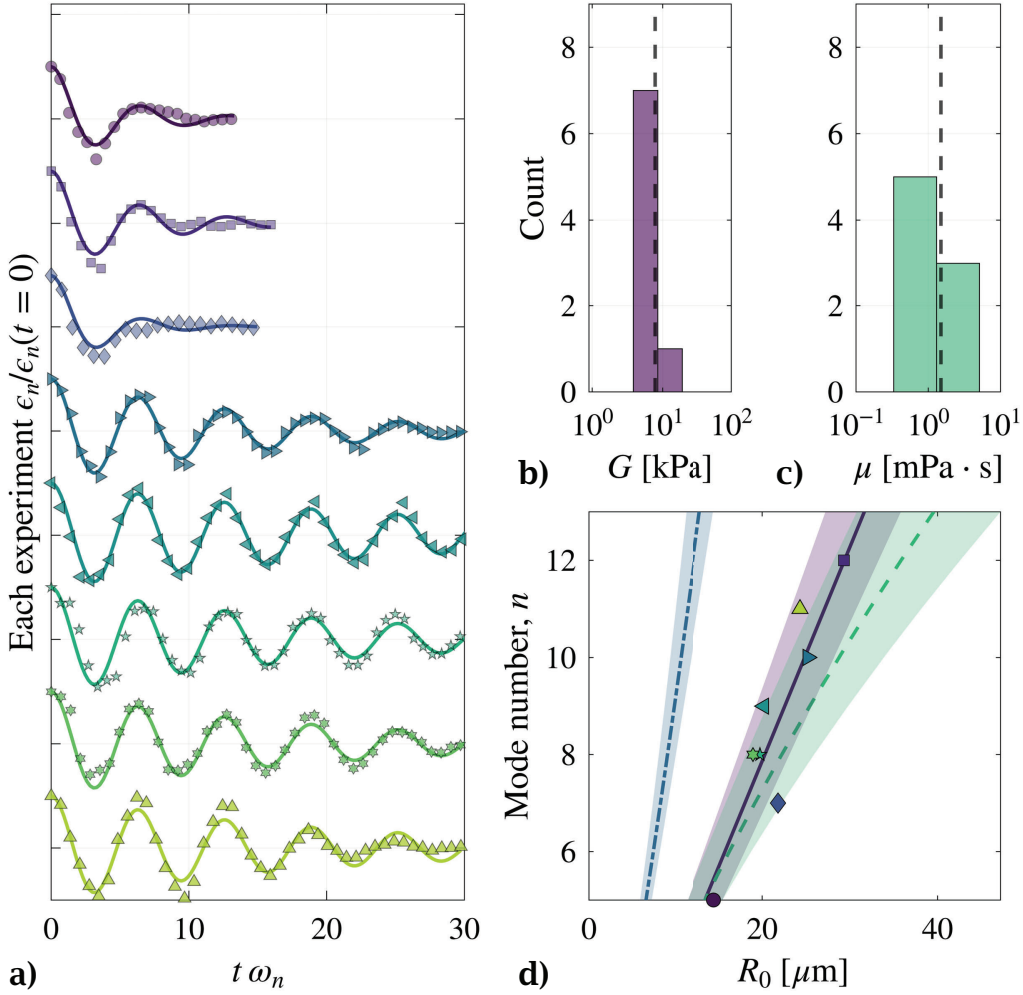


Figure 4: a) Evolution of the normalized amplitude for the most unstable mode for 10% gelatin, experimental data (symbols) and model prediction (lines), different colors correspond to different experiments. b) and c) Histograms of the calibrated shear modulus and viscosity, respectively. See [31] for all calibrated values. d) Most unstable mode as a function of equilibrium radius. Symbols and purple shaded regions/lines: present experimental data and current theory, respectively; green: Murakami et al. [24] model; and steel blue: Yang et al. [43] model. Shaded regions around the mean predictions are from using the standard deviation of the distribution of calibrated shear moduli.

and previously measured values found in the literature. For both gelatin gels in this study, the calibrated viscosity is close to that of water, $\bar{\mu}_{5\%} = 1.6 \text{ mPa} \cdot \text{s}$ and $\bar{\mu}_{10\%} = 1.5 \text{ mPa} \cdot \text{s}$ which is an order of magnitude lower than the values found in the literature [31].

Aside from the high strain rate data of [1], experiments from the literature were conducted at low (approximately quasi-static) strain rates. The study by Abeid et al. [1] showed that, using IMR, gelatin gels can become stiffer when subjected to high strain rates. However, since the material shows a range of strain rates during microcavitation rheometry, the material properties from these experiments are effectively strain- and strain-rate-averaged. For the current experiments, the strain rate can be calculated exactly using the rate of strain tensor, presented in [31]. In figure 4, $\dot{R} \approx 0$, and we assume that the perturbations are axisymmetric. Under these assumptions the maximum component

of the strain rate tensor for time and space (r, θ, ϕ) is,

$$\max_{\psi, R \approx 0} |\mathbf{D}| = \left| D_{11} \Big|_{r=\mathcal{R}(\theta=0, \phi)} \right| = (n+2) \sqrt{\frac{2n+1}{4\pi} \dot{\epsilon}_n}.$$

We then compute a time-averaged maximum strain rate,

$$\overline{D}_{\max} = \frac{1}{(n+2)} \sqrt{\frac{4\pi}{2n+1}} = \int_{t_i}^{t_f} \dot{\epsilon}_n dt = \frac{\epsilon_n(t=0)}{\Delta t},$$

where Δt is the experimental time window assuming that $\epsilon_n(\Delta t) \approx 0$. We compute this value for each experiment and find an average of $0.17 \pm 0.1 \times 10^6$ and $0.19 \pm 0.07 \times 10^6 \text{ s}^{-1}$ for the 5% and 10% gelatin gels, respectively. The discrepancy of our calibrated viscosity values compared to the literature may be due to the sustained high strain rates of these experiments, suggesting that gelatin may exhibit a strain rate dependent viscosity.

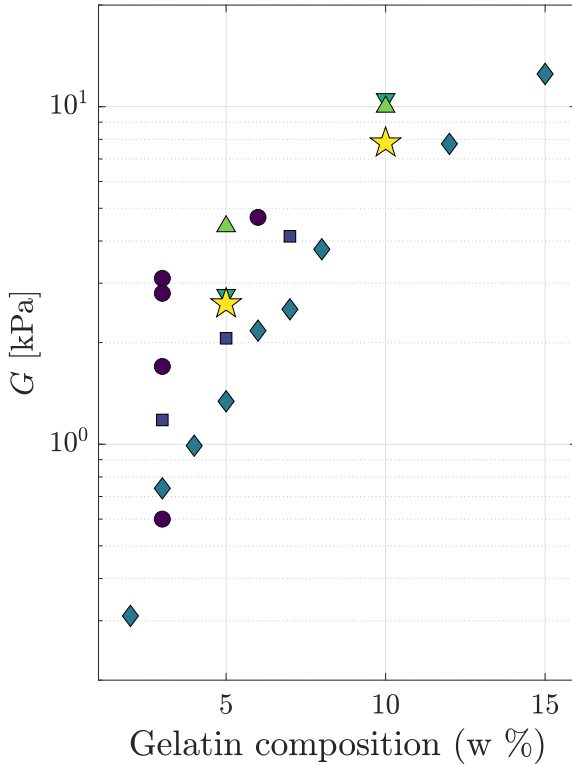


Figure 5: Shear modulus as a function of gelatin gel composition from the literature compared with current work. Purple circles: Hamaguchi and Ando [12]; dark blue squares: Yoon et al. [44]; steel blue diamonds: Bot et al. [4]; dark green downward triangles: Abeid et al. [1] quasi-static; light green upward triangles: Abeid et al. [1] high strain rate; and yellow stars: current work.

Lastly, we compare the most unstable mode predicted from the different models with the calibrated value for elasticity shown in figure 4 d). We solve the parametric instability condition with the mean and $\pm \text{std}(G)$ to generate the predictive region for each model. As expected, the experimental data lies directly within the region predicted by the present theory. Additionally, the linear experimental data suggests better agreement with the present model than the model by Murakami et al. [24].

6.2. Large amplitude radial oscillations

Four experimental trials are considered where the bubble surface exhibits small perturbations at its maximum radius [31]. Figure 6a shows one set of the radial and surface perturbation modes experimental data and calibrated model prediction. Modes in the optimization and testing data for the calibrated model are shown in frames b-f and g-h, respectively. The calibrated model agrees with experimental data before collapse.

Near the point of the collapse the perturbation prediction deviates from the experimental data. There are three explanations. First, although the perturbation amplitudes are exceedingly small, their coefficients η and ξ become large near collapse since they depend on \dot{R} and \ddot{R} . This leads to large $\dot{\epsilon}_n$ and $\ddot{\epsilon}_n$ near collapse. Higher-order models capture

interaction terms between different perturbation modes that are important when the magnitude of their time derivatives is large [35]. Secondly, since the resolution of the camera is constant, as the bubble becomes smaller, the amount of data to construct the bubble surface becomes sparse. Thirdly, through imaging, we only access a two dimensional projection of the non-spherical bubble surface and assume perturbations are within that plane. Low variability of out of plane perturbations near the maximum radius (from small values of \dot{R}) may explain the agreement early in the experiment where the radial motion is approximately a linear deviation from the maximum radius.

Introducing the non-spherical perturbations into the inverse characterization procedure refines the calibrated material property values. The present calibrated material parameters are $\bar{\alpha} = 0.083 \pm 0.048$ and $\bar{\mu} = 0.15 \pm 0.073 \text{ Pa s}$, see [31] for calibrated material properties for each dataset. The mean viscosity is within 20% of the previously calibrated value of $\mu = 0.186 \pm 0.194 \text{ Pa s}$ from Yang et al. [40]. On the other hand, the mean strain hardening parameter is over 80% different from the previously calibrated value of $\alpha = 0.48 \pm 0.14$. The discrepancy is due to calibration being limited to first collapse in the study by Yang et al. [40].

7. Conclusions

We present a model for the evolution of bubble surface instabilities within a strain stiffening viscoelastic material. In the linear radial oscillation regime and with zero shear modulus, our model agrees with the irrotational model from [30]. We compare our model to two sets of experiments, small radial oscillations from ultrasound forcing within 5% and 10% gelatin solutions and large radial oscillations from LIC in polyacrilamide. The experimental data shows a linear relationship between the most unstable mode and equilibrium radius in viscoelastic materials which is only predicted by the current theory. The LIC bubble experiments showed small surface perturbations at the maximum radius which grow throughout the collapse phase. Despite having a two-dimensional view of the bubble and modeling the perturbations in a linear fashion, agreement between the experimental data and the model is observed. We validated our model for different materials and dynamical regimes from small radial oscillations to large, inertial collapses with non-spherical perturbations. The modeling approach taken in this study can easily be applied to other material models by considering a different Cauchy stress tensor. Moreover, a single simulation of the presented current theory for the case of large radial oscillation runs on the order of about 1 minute locally (Dell Alienware x15 R2 with intel CORE-i9). In contrast, a full three-dimensional numerical simulation of the problem can exceed run times of 48 hours on 48 CPU cores (GCS Supercomputer SuperMUC-NG at Leibniz Supercomputing Centre) [26]. Future studies will investigate the use of non-spherical ultrasound forced bubbles for characterization across a range of strain rates by modulating the forcing frequency and bubble size.

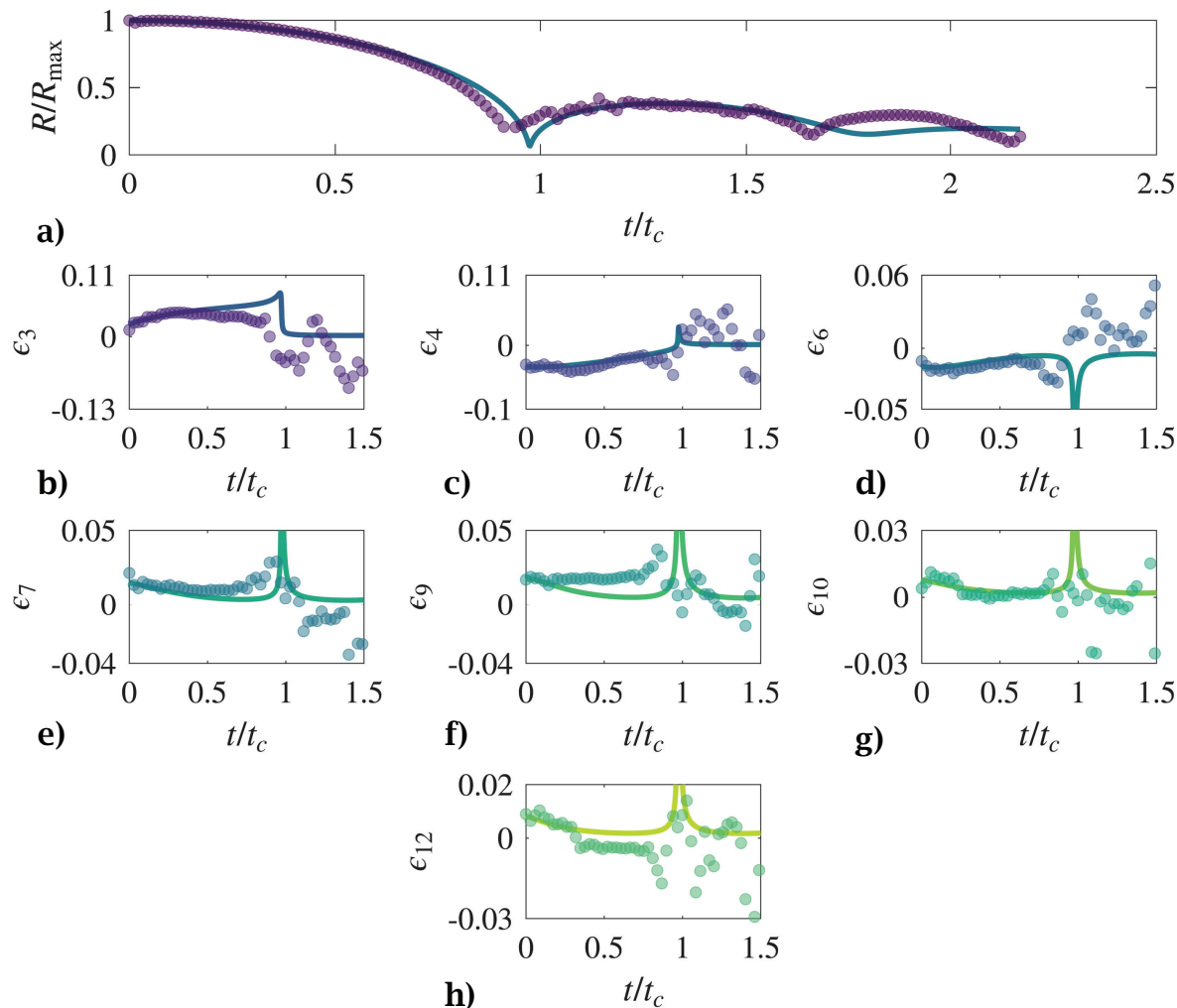


Figure 6: Non-spherical laser induced bubble **a)** mean radius evolution in time, **b-h)** third, fourth, sixth, seventh, ninth, tenth, and twelfth mode amplitude over time. Circles: experimental data; and lines: calibrated model prediction.

8. Acknowledgments

MRJ acknowledges support from the U.S. Department of Defense under the DEPSCoR program Award No. FA9550-23-1-0485 (PM Dr. Timothy Bentley). JBE, MRJ, and JY gratefully acknowledge support from the U.S. National Science Foundation (NSF) under Grant Nos. 2232426, 2232427, and 2232428, respectively. Funding agencies were not involved in study design; in the collection, analysis and interpretation of data; in the writing of the report; or in the decision to submit the article for publication. The opinions, findings, and conclusions, or recommendations expressed are those of the authors and do not necessarily reflect the views of the funding agencies.

CRediT authorship contribution statement

Sawyer Remillard: Conceptualization, Data Curation, Formal Analysis, Investigation, Methodology, Software, Validation, Writing - Original draft preparation, Writing -

review & editing. **Bachir A. Abeid:** Data Curation, Investigation, Methodology, Writing - review & editing. **Timothy L. Hall:** Methodology, Resources, Writing - review & editing. **Jonathan R. Sukovich:** Conceptualization, Methodology, Resources, Writing - review & editing. **Jacob Baker:** Writing - Original draft preparation, Writing - review & editing. **Jin Yang:** Conceptualization, Data curation, Funding Acquisition, Writing - review & editing. **Jonathan B. Estrada:** Conceptualization, Funding Acquisition, Investigation, Methodology, Resources, Supervision, Writing - review & editing. **Mauro Rodriguez Jr.:** Conceptualization, Funding Acquisition, Investigation, Methodology, Project Administration, Resources, Supervision, Writing - original draft, Writing - review & editing.

References

- [1] Abeid, B.A., Fabiilli, M.L., Aliabouzar, M., Estrada, J.B., 2024a. Experimental & numerical investigations of ultra-high-speed dynamics of optically induced droplet cavitation in soft materials. *Journal of the Mechanical Behavior of Biomedical Materials* 160, 106776.

[2] Abeid, B.A., Fabiilli, M.L., Estrada, J.B., Aliabouzar, M., 2024b. Ultra-high-speed dynamics of acoustic droplet vaporization in soft biomaterials: Effects of viscoelasticity, frequency, and bulk boiling point. *Ultrason. Sonochem.*, 106754–1–11.

[3] Bailey, M.R., Khokhlova, V.A., Sapozhnikov, O.A., Kargl, S.G., Crum, L.A., 2003. Physical mechanisms of the therapeutic effect of ultrasound (a review). *Acoustical Physics* 49, 369–388.

[4] Bot, A., van Amerongen, I.A., Groot, R.D., Hoekstra, N.L., Agterof, W.G., 1996. Large deformation rheology of gelatin gels. *Polymer Gels and Networks* 4, 189–227.

[5] Brennen, C.E., 1995. Cavitation and bubble dynamics. Oxford University Press.

[6] Brujan, E.A., Vogel, A., 2006. Stress wave emission and cavitation bubble dynamics by nanosecond optical breakdown in a tissue phantom. *Journal of Fluid Mechanics* 558, 281–308.

[7] Cleve, S., Guédra, M., Inserra, C., Mauger, C., Blanc-Benon, P., 2018. Surface modes with controlled axisymmetry triggered by bubble coalescence in a high-amplitude acoustic field. *Phys. Rev. E* 98, 033115–1–8.

[8] Estrada, J.B., Barajas, C., Henann, D.L., Johnsen, E., Franck, C., 2018. High strain-rate soft material characterization via inertial cavitation. *Journal of the Mechanics and Physics of Solids* 112, 291–317.

[9] Gaudron, R., Murakami, K., Johnsen, E., 2020. Shape stability of a gas cavity surrounded by linear and nonlinear elastic media. *J. Mech. Phys. Solids* 143, 104047.

[10] Gaudron, R., Warnez, M.T., Johnsen, E., 2015. Bubble dynamics in a viscoelastic medium with nonlinear elasticity. *J. Fluid Mech.* 766, 54–75.

[11] Guédra, M., Cleve, S., Mauger, C., Blanc-Benon, P., Inserra, C., 2017. Dynamics of nonspherical microbubble oscillations above instability threshold. *Phys. Rev. E* 96, 063104–1–8.

[12] Hamaguchi, F., Ando, K., 2015. Linear oscillation of gas bubbles in a viscoelastic material under ultrasound irradiation. *Physics of Fluids* 27, 113103–1–17.

[13] Harkin, A.A., Kaper, T.J., Nadim, A., 2013. Energy transfer between the shape and volume modes of a nonspherical gas bubble. *Physics of Fluids* 25, 062101–1–11.

[14] Hilgenfeldt, S., Lohse, D., Brenner, M.P., 1996. Phase diagrams for sonoluminescing bubbles. *Physics of Fluids* 8, 2808–2826.

[15] Johnsen, E., Colonius, T., 2009. Numerical simulations of non-spherical bubble collapse. *Journal of Fluid Mechanics* 629, 231–262.

[16] Kheiroloomoom, A., Dayton, P.A., Lum, A.F., Little, E., Paoli, E.E., Zheng, H., Ferrara, K.W., 2007. Acoustically-active microbubbles conjugated to liposomes: Characterization of a proposed drug delivery vehicle. *Journal of Controlled Release* 118, 275–284.

[17] Kikuchi, H., Keiji Sakai, K.S., Kenshiro Takagi, K.T., 1991. Surface tension wave on gelatin gel. *Japanese Journal of Applied Physics* 30, L1668–1–3.

[18] Knowles, J.K., 1977. The finite anti-plane shear field near the tip of a crack for a class of incompressible elastic solids. *International Journal of Fracture* 13, 611–639.

[19] Lajoinie, G., Luan, Y., Gelderblom, E., Dollet, B., Mastik, F., Dewitte, H., Lentacker, I., de Jong, N., Versluis, M., 2018. Non-spherical oscillations drive the ultrasound-mediated release from targeted microbubbles. *Communications Physics* 1, 1–9.

[20] Lauterborn, W., Bolle, H., 1975. Experimental investigations of cavitation-bubble collapse in the neighbourhood of a solid boundary. *Journal of Fluid Mechanics* 72, 391–399.

[21] Liu, Y., Sugiyama, K., Takagi, S., Matsumoto, Y., 2012. Surface instability of an encapsulated bubble induced by an ultrasonic pressure wave. *Journal of Fluid Mechanics* 691, 315–340.

[22] Mancia, L., Vlaisavljevich, E., Xu, Z., Johnsen, E., 2017. Predicting Tissue Susceptibility to Mechanical Cavitation Damage in Therapeutic Ultrasound. *Ultrasound Med. Biol.* 43, 1421–1440.

[23] Maxwell, A.D., Cain, C.A., Duryea, A.P., Yuan, L., Gurm, H.S., Xu, Z., 2009. Noninvasive thrombolysis using pulsed ultrasound cavitation therapy – histotripsy. *Ultrasound in Medicine & Biology* 35, 1982–1994.

[24] Murakami, K., Gaudron, R., Johnsen, E., 2020. Shape stability of a gas bubble in a soft solid. *Ultrasonics Sonochemistry* 67, 105170–1–12.

[25] Murakami, K., Yamakawa, Y., Zhao, J., Johnsen, E., Ando, K., 2021. Ultrasound-induced nonlinear oscillations of a spherical bubble in a gelatin gel. *Journal of Fluid Mechanics* 924, A38–1–17.

[26] Nagy, D., Adam, S., Hegedűs, F., 2025. Direct numerical simulation of spherical and non-spherical bubble dynamics using the alpaca compressible multiphase flow solver. *International Journal of Multiphase Flow* 191, 105287–1–24.

[27] Ogden, R.W., Sinclair, G., 1984. Non-Linear Elastic Deformations. E. Horwood, Halsted Press.

[28] Plesset, M.S., 1954. On the stability of fluid flows with spherical symmetry. *Journal of Applied Physics* 25, 96–98.

[29] Plesset, M.S., Prosperetti, A., 1977. Bubble Dynamics and Cavitation. *Annu. Rev. Fluid Mech.* 9, 145–185.

[30] Prosperetti, A., 1977. Viscous effects on perturbed spherical flows. *Q. Appl. Math.* 34, 339–352.

[31] Remillard, S., Abeid, B.A., Hall, T.L., Sukovich, J.R., Baker, J., Yang, J., Estrada, J.B., Rodriguez Jr., M., 2026. Supplementary information. *Extreme Mechanics Letters*.

[32] Saint-Michel, B., Garbin, V., 2020. Acoustic bubble dynamics in a yield-stress fluid. *Soft Matter* 16, 10405–10418.

[33] Shaw, S.J., 2006. Translation and oscillation of a bubble under axisymmetric deformation. *Physics of Fluids* 18, 072104–1–15.

[34] Shaw, S.J., 2025a. Shape deformation of a gas bubble forced by a dual frequency time-dependent pressure field. *Physics of Fluids* 37, 022128–1–11.

[35] Shaw, S.J., 2025b. Shape distortion of an acoustically forced gas microbubble. *International Journal of Multiphase Flow* 184, 105074–1–9.

[36] Tinkov, S., Winter, G., Coester, C., Bekeridjian, R., 2010. New doxorubicin-loaded phospholipid microbubbles for targeted tumor therapy: Part i — formulation development and in-vitro characterization. *Journal of Controlled Release* 143, 143–150.

[37] Versluis, M., Goertz, D.E., Palanchon, P., Heitman, I.L., van der Meer, S.M., Dollet, B., de Jong, N., Lohse, D., 2010. Microbubble shape oscillations excited through ultrasonic parametric driving. *Phys. Rev. E* 82, 026321–1–6.

[38] Vlaisavljevich, E., Lin, K.W.K.W., Warnez, M.T., Singh, R., Mancia, L., Putnam, A.J., Johnsen, E., Cain, C., Xu, Z., 2015. Effects of tissue stiffness, ultrasound frequency, and pressure on histotripsy-induced cavitation bubble behavior. *Phys. Med. Biol.* 60, 2271–2292.

[39] Xu, Z., Raghavan, M., Hall, T.L., Chang, C.W., Mycek, M.A., Fowlkes, J.B., Cain, C.A., 2007. High speed imaging of bubble clouds generated in pulsed ultrasound cavitation therapy - histotripsy. *IEEE Transactions on Ultrasonics, Ferroelectrics, and Frequency Control* 54, 2091–2101.

[40] Yang, J., Cramer, H.C., Franck, C., 2020. Extracting non-linear viscoelastic material properties from violently-collapsing cavitation bubbles. *Extreme Mechanics Letters* 39, 100839–1–6.

[41] Yang, J., Cramer III, H.C., Bremer, E.C., Buyukozturk, S., Yin, Y., Franck, C., 2022. Mechanical characterization of agarose hydrogels and their inherent dynamic instabilities at ballistic to ultra-high strain-rates via inertial microcavitation. *Extreme Mechanics Letters* 51, 101572–1–8.

[42] Yang, J., Cramer III, H.C., Franck, C., 2021a. Dynamic rugae strain localizations and instabilities in soft viscoelastic materials during inertial microcavitation, in: *Dynamic Behavior of Materials, Volume 1: Proceedings of the 2020 Annual Conference on Experimental and Applied Mechanics*, Springer. pp. 45–49.

[43] Yang, J., Tzoumaka, A., Murakami, K., Johnsen, E., Henann, D.L., Franck, C., 2021b. Predicting Complex Non-spherical Instability Shapes of Inertial Cavitation Bubbles in Viscoelastic Soft Matter. *Phys. Rev. E* 104, 045108–1–9.

[44] Yoon, S., Aglyamov, S.R., Karpouli, A.B., Kim, S., Emelianov, S.Y., 2011. Estimation of mechanical properties of a viscoelastic medium

using a laser-induced microbubble interrogated by an acoustic radiation force. *The Journal of the Acoustical Society of America* 130, 2241–2248.

1. Kinematically-consistent analytical model

The linearized deformation gradient tensor is

$$\mathbf{F} = \frac{\partial \mathbf{x}}{\partial \mathbf{x}_o} = \begin{bmatrix} \frac{\partial r}{\partial r_o} & \frac{1}{r_o} \frac{\partial r}{\partial \theta_o} & \frac{1}{r_o \sin \theta_o} \frac{\partial r}{\partial \phi_o} \\ r \frac{\partial \theta}{\partial r_o} & \frac{r_o}{r} \frac{\partial \theta}{\partial \theta_o} & \frac{r_o \sin \theta_o}{r} \frac{\partial \theta}{\partial \phi_o} \\ r \sin \theta \frac{\partial \phi}{\partial r_o} & \frac{r_o \sin \theta}{r_o} \frac{\partial \phi}{\partial \theta_o} & \frac{r_o \sin \theta_o}{r_o} \frac{\partial \phi}{\partial \phi_o} \end{bmatrix} = \begin{bmatrix} \frac{\partial(r_s + \epsilon_n r_1)}{\partial r_o} & \frac{\epsilon_n \partial r_1}{r_o \partial \theta_o} & \frac{\epsilon_n}{r_o \sin \theta_o} \frac{\partial r_1}{\partial \phi_o} \\ \epsilon_n r_s \frac{\partial \theta_1}{\partial r_o} & \frac{r_s}{r_o} + \epsilon_n \left(\frac{r_1}{r_o} + \frac{r_s}{r_o} \frac{\partial \theta_1}{\partial \theta_o} \right) & \epsilon_n \frac{r_s}{r_o \sin \theta_o} \frac{\partial \theta_1}{\partial \phi_o} \\ \epsilon_n r_s \sin \theta_o \frac{\partial \phi_1}{\partial r_o} & \epsilon_n \sin \theta_o \frac{r_s}{r_o} \frac{\partial \phi_1}{\partial \theta_o} & \frac{r_s}{r_o} + \epsilon_n \left(\frac{r_1}{r_o} + \frac{r_s}{r_o} \left(\theta_1 \cot \theta_o + \frac{\partial \phi_1}{\partial \phi_o} \right) \right) \end{bmatrix}. \quad (1)$$

The linearized deformation and inverse deformation maps are

$$r(\psi_o, t) = r_s + \epsilon_n \frac{R^{n+3}}{r_s^{n+2}} Y_n^m(\theta_o, \phi_o), \quad (2a)$$

$$\theta(\psi_o, t) = \theta_o - \epsilon_n \frac{R^{n+3}}{(n+1)r_s^{n+3}} \frac{\partial}{\partial \theta_o} Y_n^m(\theta_o, \phi_o), \quad (2b)$$

$$\phi(\psi_o, t) = \phi_o - \epsilon_n \frac{R^{n+3}}{(n+1)r_s^{n+3}} \frac{1}{\sin^2 \theta_o} \frac{\partial}{\partial \phi_o} Y_n^m(\theta_o, \phi_o). \quad (2c)$$

$$r_o(\psi, t) = o - \epsilon_n \frac{R^{n+3}}{r^n \varrho^2} Y_n^m, \quad (3a)$$

$$\theta_o(\psi, t) = \theta + \epsilon_n \frac{R^{n+3}}{(n+1)r^{n+3}} \frac{\partial}{\partial \theta} Y_n^m, \quad (3b)$$

$$\phi_o(\psi, t) = \phi + \epsilon_n \frac{R^{n+3}}{(n+1)r^{n+3}} \frac{1}{\sin^2 \theta} \frac{\partial}{\partial \phi} Y_n^m, \quad (3c)$$

respectively, where $\varrho = (r^3 - R^3 + R_o^3)^{1/3}$. The linearized Eulerian velocity and acceleration are

$$v_r = \frac{R^2 \dot{R}}{r^2} + \frac{R^{n+2}}{r^{n+5}} \left(\epsilon_n \dot{R} \left((n+3)r^3 - nR^3 \right) + r^3 R \dot{\epsilon}_n \right) Y_n^m, \quad (4a)$$

$$v_\theta = -\frac{R^{n+2}}{(n+1)r^{n+5}} \left(\epsilon_n \dot{R} (n+3) (r^3 - R^3) + r^3 R \dot{\epsilon}_n \right) \frac{\partial Y_n^m}{\partial \theta}, \quad (4b)$$

$$v_\phi = \frac{R^{n+2}}{\sin \theta (n+1)r^{n+5}} \left(\epsilon_n \dot{R} (n+3) (r^3 - R^3) + r^3 R \dot{\epsilon}_n \right) \frac{\partial Y_n^m}{\partial \phi}, \quad (4c)$$

$$a_r = \frac{2R\dot{R}^2 + R^2\ddot{R}}{r^2} - \frac{2R^4\dot{R}^2}{r^5} + \frac{R^{n+1}}{r^{n+8}} \left[r^3 R \left(\epsilon_n \left((n+3)r^3 - nR^3 \right) \ddot{R} + r^3 R \ddot{\epsilon}_n \right) + 2r^3 R \dot{R} \dot{\epsilon}_n \left((n+3)r^3 - (n+2)R^3 \right) + \epsilon_n \dot{R}^2 \left((n+2)(n+3)r^6 - 2(n(n+6) + 6)r^3 R^3 + n(n+7)R^6 \right) \right] Y_n^m, \quad (5a)$$

$$a_\theta = -\frac{R^{n+1}}{(n+1)r^{n+8}} \left(\epsilon_n(n+3)(r^3 - R^3) \left(((n+2)r^3 - (n+4)R^3) \dot{R}^2 + r^3 R \ddot{R} \right) \right. \\ \left. + r^3 R \left(2((n+3)r^3 - (n+2)R^3) \dot{R} \dot{\epsilon}_n + r^3 R \ddot{\epsilon}_n \right) \right) \frac{\partial Y_n^m}{\partial \theta}, \quad (5b)$$

$$a_\phi = -\frac{R^{n+1}}{\sin \theta (n+1)r^{n+8}} \left(\epsilon_n(n+3)(r^3 - R^3) \left(((n+2)r^3 - (n+4)R^3) \dot{R}^2 + r^3 R \ddot{R} \right) \right. \\ \left. + r^3 R \left(2((n+3)r^3 - (n+2)R^3) \dot{R} \dot{\epsilon}_n + r^3 R \ddot{\epsilon}_n \right) \right) \frac{\partial Y_n^m}{\partial \phi}. \quad (5c)$$

1.1. Linearized quantities for momentum balance

The left Cauchy-Green deformation tensor given the linearized deformation is

$$\mathbf{B} = \begin{bmatrix} B_{11} & B_{12} & B_{13} \\ B_{12} & B_{22} & B_{23} \\ B_{13} & B_{23} & B_{33} \end{bmatrix}, \quad (6)$$

where

$$B_{11} = \frac{\rho^4}{r^4} - 2\epsilon_n \rho \frac{R^{n+3} \left((n+2)r^3 + n(R_o^3 - R^3) \right)}{r^{n+7}} Y_n^m, \quad (7a)$$

$$B_{12} = \epsilon_n \frac{R^{n+3}}{r^{n+7}} \left(\frac{(n+3)\rho^4}{n+1} + \frac{r^6}{\rho^2} \right) \frac{\partial Y_n^m}{\partial \theta}, \quad (7b)$$

$$B_{13} = \epsilon_n \frac{R^{n+3}}{r^{n+7}} \left(\frac{(n+3)\rho^4}{n+1} + \frac{r^6}{\rho^2} \right) \csc \theta \frac{\partial Y_n^m}{\partial \phi}, \quad (7c)$$

$$B_{22} = \frac{r^2}{\rho^2} + 2\epsilon_n \frac{R^{n+3}}{r^{n+1}} \left(\frac{r^3}{\rho^5} Y_n^m - \frac{1}{(n+1)\rho^2} \frac{\partial^2 Y_n^m}{\partial \theta^2} \right), \quad (7d)$$

$$B_{23} = \frac{2\epsilon_n R^{n+3}}{(n+1)r^{n+1}\rho^2} \csc \theta \left(\cot \theta \frac{\partial Y_n^m}{\partial \phi} - \frac{\partial^2 Y_n^m}{\partial \theta \partial \phi} \right), \quad (7e)$$

$$B_{33} = \frac{r^2}{\rho^2} + 2\epsilon_n \frac{R^{n+3}}{r^{n+1}} \left(\frac{(n+1)r^3 + n(R_o^3 - R^3)}{\rho^5} Y_n^m + \frac{1}{(n+1)\rho^2} \frac{\partial^2 Y_n^m}{\partial \theta^2} \right). \quad (7f)$$

Using the Eulerian velocity, we can take the spatial gradient and average it with its transpose to obtain the rate of strain tensor,

$$\mathbf{D} = \begin{bmatrix} D_{11} & D_{12} & D_{13} \\ D_{12} & D_{22} & D_{23} \\ D_{13} & D_{23} & D_{33} \end{bmatrix}, \quad (8)$$

where

$$D_{11} = -\frac{2R^2 \dot{R}}{r^3} - \frac{R^{n+2}}{r^{n+6}} \left(((n+2)(n+3)r^3 - n(n+5)R^3) \epsilon_n \dot{R} + (n+2)r^3 R \dot{\epsilon}_n \right) Y_n^m, \quad (9a)$$

$$D_{12} = \frac{R^{n+2}}{2(n+1)r^{n+6}} \left(((n+2)(n+3)r^3 - (n(n+5)+9)R^3) \epsilon_n \dot{R} + (n+2)r^3 R \dot{\epsilon}_n \right) \frac{\partial Y_n^m}{\partial \theta}, \quad (9b)$$

$$D_{13} = \frac{R^{n+2}}{2(n+1)r^{n+6}} \left(((n+2)(n+3)r^3 - (n(n+5)+9)R^3) \epsilon_n \dot{R} + (n+2)r^3 R \dot{\epsilon}_n \right) \csc \theta \frac{\partial Y_n^m}{\partial \phi}, \quad (9c)$$

$$D_{22} = \frac{R^2 \dot{R}}{r^3} + \frac{R^{n+2}}{r^{n+6}} \left[((n+3)r^3 - nR^3) \epsilon_n \dot{R} + r^3 R \dot{\epsilon}_n \right] Y_n^m - \frac{1}{n+1} \left((n+3)\epsilon_n(r^3 - R^3) \dot{R} + r^3 R \dot{\epsilon}_n \right) \frac{\partial^2 Y_n^m}{\partial \theta^2}, \quad (9d)$$

$$D_{23} = \frac{R^{n+2}}{(n+1)r^{n+6}} \csc \theta \left((n+3)\epsilon_n(r^3 - R^3) \dot{R} + r^3 R \dot{\epsilon}_n \right) \left(\cot \theta \frac{\partial Y_n^m}{\partial \phi} - \frac{\partial^2 Y_n^m}{\partial \theta \partial \phi} \right), \quad (9e)$$

$$D_{33} = \frac{R^2 \dot{R}}{r^3} + \frac{R^{n+2}}{r^{n+6}} \left(\epsilon_n \dot{R} \left((n+1)(n+3)r^3 - n(n+4)R^3 \right) + (n+1)r^3 R \dot{\epsilon}_n \right) Y_n^m + \frac{1}{n+1} \left((n+3)\epsilon_n(r^3 - R^3) \dot{R} + r^3 R \dot{\epsilon}_n \right) \frac{\partial^2 Y_n^m}{\partial \theta^2}. \quad (9f)$$

For the calculation of the strain rates that the material undergoes during the experiment, we evaluate the rate of strain tensor at the bubble wall,

$$\mathbf{D}|_{r=\mathcal{R}(\theta,\phi)} = \begin{bmatrix} D_{11} & D_{12} & D_{13} \\ D_{12} & D_{22} & D_{23} \\ D_{13} & D_{23} & D_{33} \end{bmatrix}_{r=\mathcal{R}(\theta,\phi)}, \quad (10)$$

where

$$D_{11}|_{r=\mathcal{R}(\theta,\phi)} = -\frac{2\dot{R}}{R} - (n+2)\dot{\epsilon}_n Y_n^m, \quad (11a)$$

$$D_{12}|_{r=\mathcal{R}(\theta,\phi)} = \frac{-3\epsilon_n \dot{R} + (n+2)R \dot{\epsilon}_n}{(n+1)R} \frac{\partial Y_n^m}{\partial \theta}, \quad (11b)$$

$$D_{13}|_{r=\mathcal{R}(\theta,\phi)} = \frac{-3\epsilon_n \dot{R} + (n+2)R \dot{\epsilon}_n}{(n+1)R} \frac{1}{\sin \theta} \frac{\partial Y_n^m}{\partial \phi}, \quad (11c)$$

$$D_{22}|_{r=\mathcal{R}(\theta,\phi)} = \frac{\dot{R}}{R} + \dot{\epsilon}_n \left(Y_n^m - \frac{1}{n+1} \frac{\partial^2 Y_n^m}{\partial \theta^2} \right), \quad (11d)$$

$$D_{23}|_{r=\mathcal{R}(\theta,\phi)} = \frac{\dot{\epsilon}_n}{(n+1) \sin \theta} \left(\cot \theta \frac{\partial Y_n^m}{\partial \phi} - \frac{\partial^2 Y_n^m}{\partial \phi \partial \theta} \right), \quad (11e)$$

$$D_{33}|_{r=\mathcal{R}(\theta,\phi)} = \frac{\dot{R}}{R} + \frac{\dot{\epsilon}_n}{(n+1)} \left((n+1)^2 Y_n^m - \frac{\partial^2 Y_n^m}{\partial \theta^2} \right), \quad (11f)$$

1.2. Coefficients for perturbation evolution equation

The damping coefficient and squared natural frequency for the non-linear perturbation evolution equation are

$$\eta = \frac{4(5+2n)}{(4+n)} \frac{\dot{R}}{R} + \frac{2(n+1)(n+2)}{\rho R^2} \mu, \quad (12)$$

$$\xi = 6 \frac{n+2}{n+4} \frac{\dot{R}^2}{R^2} - \frac{n^2-n-8}{n+4} \frac{\ddot{R}}{R} + \frac{n(n+1)(7n+20)}{(n+6)\rho R^3} \mu + \frac{(n+1)(n-1)(n+2)\gamma}{\rho R^3} + \xi_{nH} G + \xi_\alpha \alpha G, \quad (13)$$

where

$$\begin{aligned} \xi_{nH} = & \frac{n+1}{\lambda^{11}(n+6)(n+9)(n+12)\rho R_o^2} \left[2\lambda^5 (n^3 + 27n^2 + 234n + 648) (-\lambda^6 + 2\lambda^3 + n + 1) \right. \\ & + \lambda^3(\lambda^3 - 1)(n + 13) \left(108\lambda^6 + (3\lambda^3 - 1)n^3 + (2\lambda^6 + 35\lambda^3 - 9)n^2 + 2(15\lambda^6 + 43\lambda^3 - 7)n \right) \\ & \times {}_2F_1 \left[-\frac{1}{3}, \frac{n}{3} + 4; \frac{n}{3} + 5; 1 - \frac{1}{\lambda^3} \right] + (\lambda^3 - 1) \left(-108\lambda^9 + (\lambda^3 - 1)^2 n^4 + (16\lambda^6 - 37\lambda^3 + 19)n^3 \right. \\ & \left. \left. + (-30\lambda^9 + 54\lambda^6 - 266\lambda^3 + 140)n + (-2\lambda^9 + 69\lambda^6 - 199\lambda^3 + 104) + n^2 \right) {}_2F_1 \left[\frac{2}{3}, \frac{n}{3} + 4; \frac{n}{3} + 5; 1 - \frac{1}{\lambda^3} \right] \right], \end{aligned} \quad (14)$$

and

$$\begin{aligned} \xi_\alpha = & \frac{n+1}{\lambda^{10}\rho R_o} \left[2(2\lambda^6 - 3\lambda^4 + 2\lambda^3 + 3) (\lambda^3 - 1)^2 + 2(\lambda^6 - 3\lambda^4 + 2) (2\lambda^3 + n) + \frac{\lambda^2}{(n+6)(n+9)(n+12)} \left(\frac{1}{\lambda^3} - 1 \right) \right. \\ & \times \left[3(-2\lambda^9(n+6)(n+9) + \lambda^6 n(n+1)(n+6)(n+9) - \lambda^3 n(n+2)(n+7)(2n+19) + n(n+2)(n+7)(n+10)) \right. \\ & \times {}_2F_1 \left[\frac{2}{3}, \frac{n}{3} + 4; \frac{n}{3} + 5; 1 - \frac{1}{\lambda^3} \right] - \lambda^3 \left(3(n+13) (-2\lambda^6(n+6)(n+9) - \lambda^3 n(n(3n+35) + 86) + n(n+2)(n+7)) \right. \\ & \times {}_2F_1 \left[-\frac{1}{3}, \frac{n}{3} + 4; \frac{n}{3} + 5; 1 - \frac{1}{\lambda^3} \right] + (n+14) \left(4\lambda^9(n+6)(n+9) + 2\lambda^6(n+1)(n+2)(n+6)(n+9) \right. \\ & \left. - \lambda^3(n(n(4n+59) + 229) + 120) - 324) + n(n(n(2n+33) + 175) + 318) \right) {}_2F_1 \left[-\frac{2}{3}, \frac{n}{3} + 4; \frac{n}{3} + 5; 1 - \frac{1}{\lambda^3} \right] \left. \right) \\ & + 2 \left(4\lambda^{12}(n+6)(n+9) + 2\lambda^9(n+1)(n+2)(n+6)(n+9) + \lambda^6(n+1)(n+6)(n+9)(n(n+6) + 6) \right. \\ & \left. - \lambda^3 n(n(n(2n+25) + 427) + 1411) + 1398) + n(n+2)(n+11)(n(n+13) + 39) \right) {}_2F_1 \left[\frac{1}{3}, \frac{n}{3} + 4; \frac{n}{3} + 5; 1 - \frac{1}{\lambda^3} \right] \left. \right], \end{aligned} \quad (15)$$

where ${}_2F_1 [\cdot]$ is the gaussian hypergeometric function.

1.3. Coefficients for perturbation evolution equation, Yang et. al.

The work by both Yang et al. [7] and Murakami et al. [5] is formulated in terms of dimensional perturbation amplitude. For consistency, we consider the dimensional amplitude $a_n = \epsilon_n R$. The Yang et al. [7] model coefficients are

$$\eta = 5 \frac{\dot{R}}{R} + 4 \frac{\mu}{\rho R^2} + \frac{n(n+1)\mu}{3\rho R^2}, \quad (16)$$

$$\begin{aligned} \xi = & 2 \frac{\ddot{R}}{R} + 3 \frac{\dot{R}^2}{R^2} + \frac{n(n+1)\dot{R}\mu}{\rho R^3} + \frac{(n+2)(n-1)\gamma}{\rho R^3} + \frac{G}{\rho R_o^2} \left(\frac{n(n+1)}{\lambda^2 + \lambda + 1} + \frac{2(1 + \lambda^3)}{\lambda^6} \right) + \frac{G\alpha(\lambda - 1)^2}{5\rho R_o^2(\lambda^2 + \lambda + 1)\lambda^{10}} \\ & \times \left[10(n(n+1) + 2)\lambda^9 + 6(n(n+1) + 10)\lambda^8 + 3(n(n+1) + 30)\lambda^7 + (n(n+1) + 110)\lambda^6 + 120\lambda^5 + 120\lambda^4 \right. \\ & \left. + 100\lambda^3 + 60\lambda^2 + 30\lambda + 10 \right]. \end{aligned} \quad (17)$$

After linearization,

$$\eta_l = \frac{(n(n+1)+12)\mu}{3\rho R_o^2}, \quad \xi_l = \omega_n^2 = \frac{(n(n+1)+12)G}{3\rho R_o^2} + \frac{(n+2)(n-1)\gamma}{\rho R_o^3}. \quad (18)$$

1.4. Coefficients for perturbation evolution equation, Murakami et. al.

The work done by Murakami et al. [5] does not include the strain stiffening analysis. However, the deformation mapping for the computation of the Cauchy-Stress tensor matches the deformation mapping used in Yang et al. [7]. We incorporate these terms into the theory developed by Murakami et al. [5] to obtain the following coefficients,

$$\eta = 5\frac{\dot{R}}{R} + 2\frac{(n+1)(n+2)\mu}{\rho R^2} \quad (19)$$

$$\begin{aligned} \xi = & (2-n)\frac{\ddot{R}}{R} + 3\frac{\dot{R}^2}{R} + 6\frac{n(n+1)\dot{R}\mu}{\rho R^3} + \frac{(n+2)(n+1)(n-1)\gamma}{\rho R^3} + \frac{G(n+1)}{\rho R_o^2} \left(\frac{n(n+1)}{\lambda^2 + \lambda + 1} + \frac{2(1+\lambda^3)}{\lambda^6} \right) \\ & + \frac{G\alpha(n+1)(\lambda-1)^2}{5\rho R_o^2(\lambda^2 + \lambda + 1)\lambda^{10}} \left[10(n(n+1)+2)\lambda^9 + 6(n(n+1)+10)\lambda^8 + 3(n(n+1)+30)\lambda^7 + (n(n+1)+110)\lambda^6 \right. \\ & \left. + 120\lambda^5 + 120\lambda^4 + 100\lambda^3 + 60\lambda^2 + 30\lambda + 10 \right], \end{aligned} \quad (20)$$

After linearization,

$$\eta_l = \frac{2(n+2)(n+1)\mu}{\rho R_o^2}, \quad \xi_l = \omega_n^2 = \frac{(n+1)(n(n+1)+12)G}{3\rho R_o^2} + \frac{(n+2)(n+1)(n-1)\gamma}{\rho R_o^3}. \quad (21)$$

1.5. Vorticity Equation

Taking the curl of the the momentum balance, there are non-zero terms for the θ and ϕ components. Projecting each equation into their respective spherical harmonic basis, a single equation representative of the vorticity equation is

$$\begin{aligned} 3\rho \frac{R^{n+4}}{r^{n+9}} & \left(\epsilon_n \left(\dot{R}^2 \left((n+5)r^3 - (n+7)R^3 \right) + r^3 R \ddot{R} \right) + r^3 R \dot{R} \dot{\epsilon}_n \right) = \frac{R^{n+3}}{\rho^7 r^{n+13}} \\ & \times \left(\zeta G \left(\alpha \left(\zeta (4n^2 + n - 177) r^9 - \zeta^4 (n-6)(n+11) + 15(n+3)r^{12} - 8\zeta^2(n(n+3) - 36)r^6 \right. \right. \right. \\ & \left. \left. \left. + \zeta^3(n(5n+21) - 222)r^3 \right) - (3\alpha-1)\rho^2 r^4 \left(3\zeta^2(n+7) + 5(n+3)r^6 - \zeta(7n+37)r^3 \right) \right) + 30\mu(n+3)\rho^7 r^5 R^2 \dot{R} \right) \end{aligned} \quad (22)$$

where, $\zeta = R_o^3 (\lambda^3 - 1)$.

2. Non-spherical laser-induced inertial cavitation setup

Nonspherical bubbles were captured in the laser-induced inertial cavitation (LIC) experiments as described in Yang et al. [6]. Polyacrylamide hydrogel was used with an equilibrium shear modulus of 2.77 kPa. 40% acrylamide solution and 2% bis solution (Bio-Rad, Hercules, CA) were mixed to a final concentration of 8.0%/0.08% Acrylamide/Bis (v/v) and cross-linked with 0.5% Ammonium Persulfate (APS) and 1.25% N,N,N',N'-tetramethylmethane-1,2-diamine (TEMED) (ThermoFisher Scientific, USA). Single microcavitation bubbles were generated in these polyacrylamide hydrogels using a 6 ns pulse from an adjustable 1-25 mJ Q-switched 532 nm Nd:YAG laser (Continuum Minilite II, Milpitas, CA). Laser pulses are beam-expanded then pass through the back of a Nikon Ti:Eclipse microscope (Nikon Instruments, Long Island, NY) and fill the back aperture of a Nikon Plan Fluor 20X/0.5 NA objective. A dichroic mirror (Semrock, Rochester, NY) was used to pass the 532 nm beam-expanded laser light to the imaging objective and reflect the longer 640 nm illumination light from a SI-LUX640 laser illumination system (Specialized Imaging, Pitstone, United Kingdom) into a Kirana5M high-speed camera (Specialized Imaging, Pitstone, United Kingdom). Cavitation bubbles were recorded at 2×10^6 frames per second by synchronizing a 500 ns exposure time from the camera with 250 ns illumination pulse widths from the SI-LUX illumination system before laser exposure to the sample. Cavitation bubbles were generated consistently at 600 μm above the bottom surface and separated from edges and bubbles by at least 1 mm.

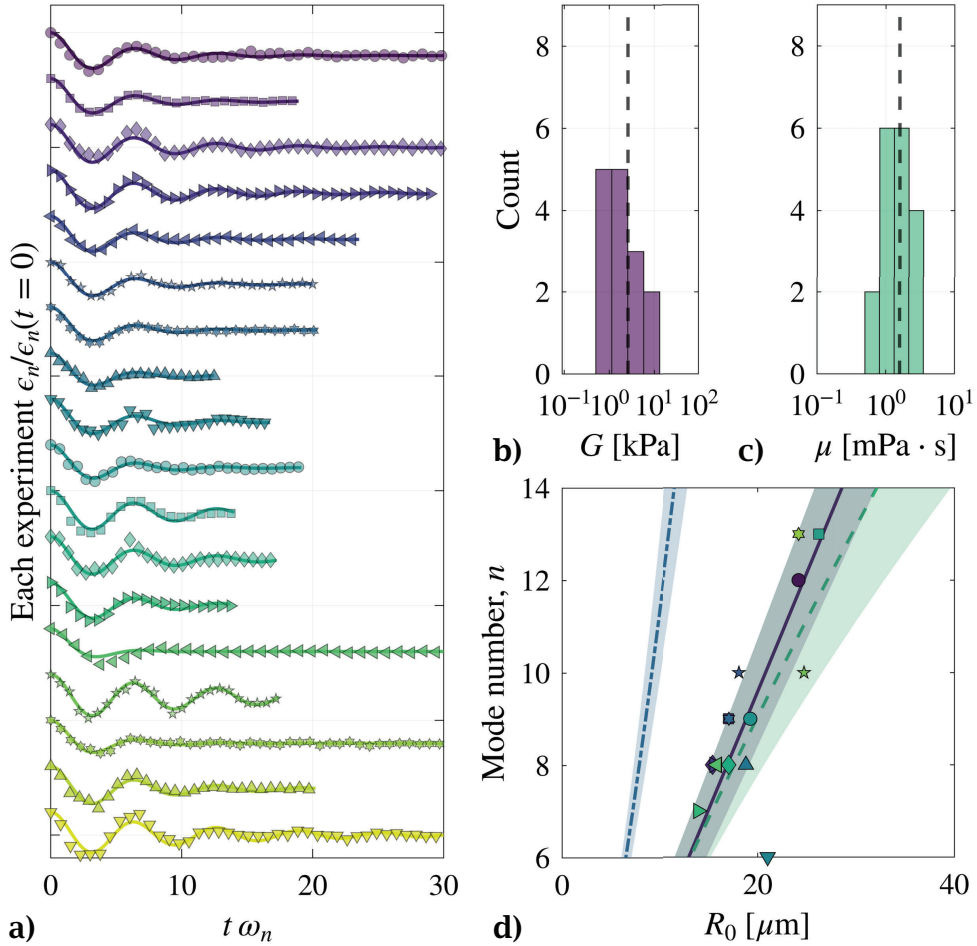


Figure 1: a) Evolution of the normalized amplitude for the most unstable mode for 5% gelatin, experimental data (symbols) and model prediction (lines), different colors correspond to different experiments. b) and c) Histograms of the calibrated shear modulus and viscosity respectively. d) Most unstable mode as a function of equilibrium radius. Symbols and purple shaded regions/lines: present experimental data and current theory, respectively; green: Murakami et al. [5] model; and steel blue: Yang et al. [7] model. Shaded regions around the mean predictions are from using the standard deviation of the distribution of extracted shear moduli.

3. Data Processing

A Fourier transform of the bubble surface data points is taken to extract the perturbation amplitudes. For the case of ultrasound forced experiments, we assume that the bubble surface is axis-symmetric, in contrast, in the non-spherical LIC experiments we observe formation of non-axisymmetric instabilities [7]. The Fourier basis is different from the spherical harmonic basis. We solve the linear problem corresponding to the transformation at each frame. In the non-axisymmetric case, since we are assuming that we are imaging at a constant value of θ , the bases are different by a constant factor of $(-1)^{|m|} \sqrt{2} \sqrt{\frac{2n+1}{4\pi} \frac{(l-|m|)!}{(l+|m|)!}} P_n^m(0)$.

We consider the dominant mode to be the mode which yields the largest root mean square deviation of the perturbation amplitude in time,

$$\text{RMSD}_n = \sqrt{\frac{1}{t_f - t_i} \int_{t_i}^{t_f} (\epsilon_n - \bar{\epsilon}_n)^2 dt}. \quad (23)$$

The dominant mode perturbation data is trimmed such that the initial condition coincides with a peak in the perturbation amplitude. Signals are rejected if $|\epsilon_n(t=0)| < 0.01$, are less than one period of oscillation, and modes which are approximately zero. Taking a Fourier transform of the signal in time, signals are rejected if they exhibit a dominant oscillation frequency which is further than 33% from half the forcing frequency (i.e., the parametric resonance condition).

A small amount of smoothing via a Savitzky-Golay filter is applied to the non-spherical LIC data to retain the signal and reduce the noise. We include perturbation data up to the point of collapse since non-linearities in the perturbation become

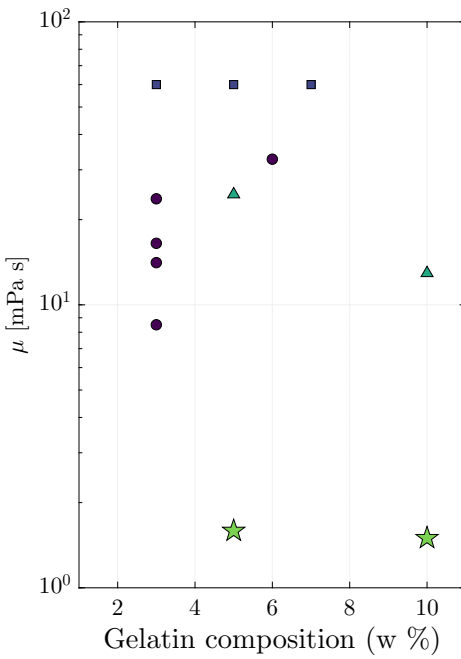


Figure 2: Shear modulus as a function of gelatin gel composition from the literature compared with present work. Purple circles: Hamaguchi and Ando [3]; blue squares: Yoon et al. [8]; green upward triangles: Abeid et al. [1] high strain rate; and green stars: present work.

dominant afterwards. A minimum norm criterion is set on the perturbation amplitude, $\|\epsilon_n\|/K^c > 10^{-3}$, where K^c is the number of frames captured between the point of maximum bubble expansion and the collapse time and $\|\cdot\|$ is the Euclidean norm.

3.1. Inverse characterization

A global search method (bayesopt) hybridized with a local search method (lsqcurvefit) in MATLAB is used to optimize the present model to the experimental data about the material properties μ , G , and α . For large radial oscillations, G is the quasi-static value, for the polyacrylamide gel in the cavitation experiments, $G_\infty = 2.77$ kPa, and therefore is omitted from the optimization. bayesopt is used to search the entire parameter space quickly. The best performing points are used in lsqcurvefit for fine grained refinement. The set of parameters with the lowest value of the loss function are the calibrated parameters for the given experiment.

The ultrasound forced experiments contain small radial oscillations. Thus, we use the analytical solution of the perturbation decay for the fitting process. η_1 depends only on viscosity, μ , and ξ_1 depends on G and γ . Optimizing for surface tension creates a non-unique solution for a given experiment with associated n and R_o : an increase in G and decrease in γ (or vice versa) will lead to the same value for ξ_1 . Thus, the surface tension is quantity that is set rather than optimized. For the gelatin gels analyzed via ultrasound forcing, surface tension will be set to 32 mN/m [4]. For the polyacrylamide gels analyzed via LIC, we use the value from [7] of 56 mN/m. We sweep over three orders of magnitude for stiffness and viscosity with bounds of [0.1, 100] kPa and [0.1, 100] mPa s, respectively. The loss function for the ultrasound-forced data is set to the RMSE between the experimentally obtained dominant mode perturbation amplitude as a function of time and the values predicted by the model. After extracting the optimal parameters to fit the dataset, we computed the R^2 value between the predicted data and the experimental data. We reject datasets with $R^2 < 0.75$.

The full coupled system is solved to calibrate the non-spherical LIC experimental data. The Keller-Miksis equation is solved for the radial dynamics with the associated coupled equations for thermal and mass transport as described in [2]. The compressive, thermal, and mass transport effects are small compared to the inertial and constitutive effects and therefore are generate $\mathcal{O}(\epsilon_n^2)$ in the perturbation dynamics. The parameters α and μ are optimized through minimizing the loss function equation (24) with bounds $[10^{-3}, 10]$ and $[10^{-3}, 1]$ Pa s, respectively.

The optimization problem involves each mode perturbation amplitude as an objective for each instance in time. We normalize the radial data and each mode's perturbation amplitude data by its respective Euclidean norm. To avoid multi-objective optimization, we construct a scalar loss function where the radial error is multiplied by the number of modes

Table 1

Summary of calibrated material properties to each experimental dataset for the ultra-sound forced experiments.

Experiment #	Gel (wt%)	Elasticity, G [kPa]	Viscosity, μ [Pa s]
1	5	2.53	1.48
2	5	0.77	1.45
3	5	0.77	0.91
4	5	0.99	0.88
5	5	3.14	1.52
6	5	0.50	1.42
7	5	0.97	1.64
8	5	2.86	2.38
9	5	12.86	3.48
10	5	2.22	1.92
11	5	3.74	1.05
12	5	1.86	1.07
13	5	1.26	1.24
14	5	0.50	2.68
15	5	1.19	0.50
16	5	9.64	3.41
17	5	0.62	1.01
18	5	0.50	0.58
1	10	7.82	2.44
2	10	8.36	1.96
3	10	18.41	5.04
4	10	8.16	0.80
5	10	4.48	0.33
6	10	5.72	0.48
7	10	5.65	0.51
8	10	3.89	0.44

Table 2

Summary of calibrated material properties to each experimental dataset for the non-spherical LIC experiments.

Experiment #	Strain-stiffening elasticity, α [-/-]	Viscosity, μ [mPa·s]
1	0.040	91.1
2	0.056	181.2
3	0.147	89.9
4 (main manuscript)	0.090	240.1

considered and summed with the perturbation error. The scalar error function is

$$\mathcal{E} = \left(\sum_k^K \left[\frac{N}{\|R^{\text{exp}}\|} (R^{\text{exp}}(t_k) - R^{\text{sim}}(t_k)) \right]^2 + \sum_n^N \sum_k^{K^c} \left[\frac{1}{\|\epsilon_n^{\text{exp}}\|} (\epsilon_n^{\text{exp}}(t_k) - \epsilon_n^{\text{sim}}(t_k)) \right]^2 \right)^{1/2}, \quad (24)$$

where superscripts exp and sim denote experimental and simulated values, respectively. N is the total number of modes considered from the experiment, k a summation over time-frames in the experiment, and K the total number of frames in the experiment. The loss function is implemented into *bayesopt* and *lsqcurvefit* in MATLAB.

The results from applying the optimization procedure to the LIC experimental data are shown in figure 3, figure 4, and figure 5. Modes (3, 4, 7, 9, 10, 12, 13), (3, 4, 6, 7), (2) from the first, second, and third experiments respectively passed the pre-filtering criteria to be included in the optimization. We observe agreement between the dynamics of additional modes not included in the optimization. In figure 4 and figure 5, we also plot modes (9) and (3) for experiments two and three, respectively. From the first experiment, the modes presented were included in the optimization. As seen in table 3, when these added modes (not included in the optimization procedure) are used to compute the loss function, we achieve a reduction in the scalar value. This suggests successful model calibration.

4. Inverse characterization consistency check

We test our inverse characterization method on synthetic data that resembles the ultrasound forced datasets. The data was generated with a shear modulus of $G = 4$ kPa, and a viscosity of $\mu = 1$ mPa s. Gaussian noise was injected into the

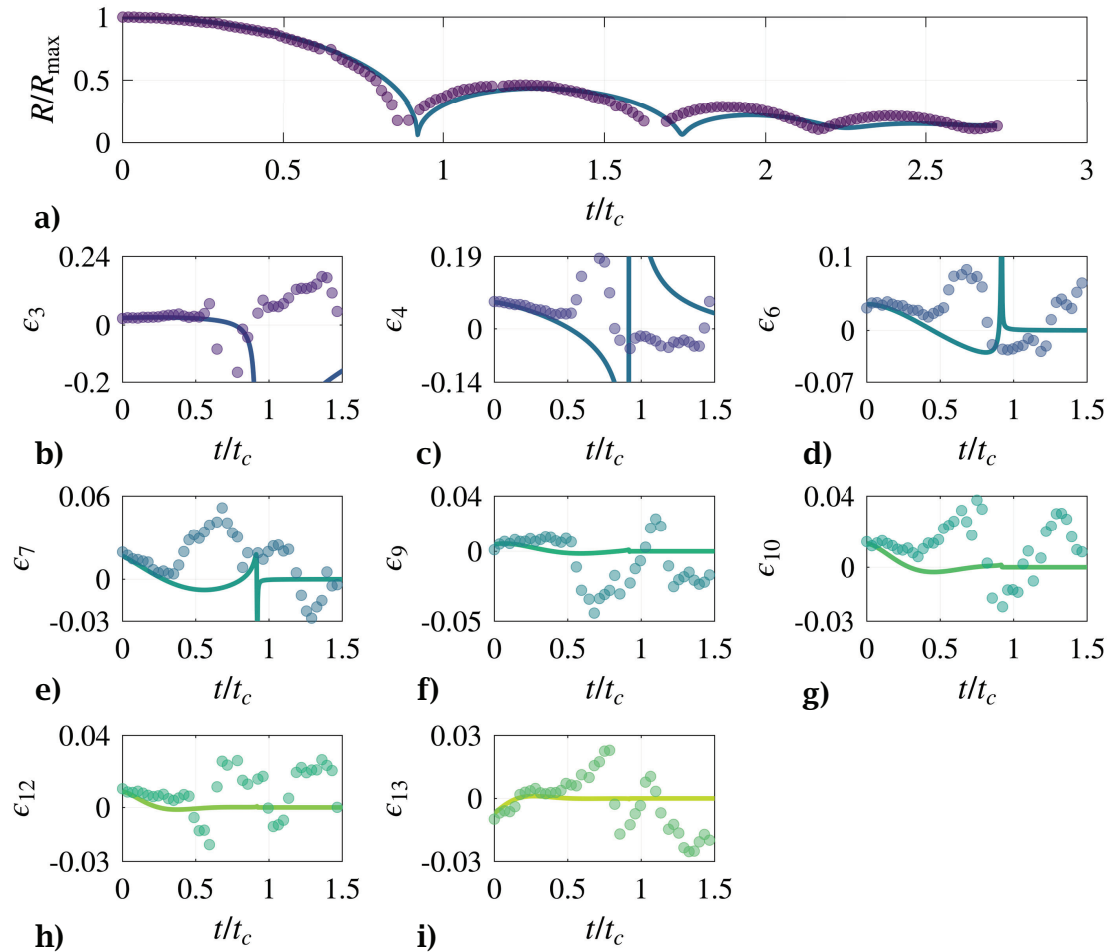


Figure 3: Experiment 1. Non-spherical laser induced bubble **a)** mean radius evolution in time, **b-i)** third, fourth, sixth, seventh, ninth, tenth, twelfth, and thirteenth mode perturbation amplitude over time. Circles: experimental data; and lines: calibrated model prediction.

Experiment	\mathcal{E} from optimization	\mathcal{E} with additional modes
1	0.275	-
2	0.160	0.151
3	0.5041	0.402
4 (main manuscript)	0.167	0.156

Table 3

Summary of loss function values from model calibration to the LIC experimental data. Values are reported from the optimization procedure as well as when additional modes are included.

perturbation amplitude at each timestep, the frequency of oscillation, and the equilibrium radius which was calculated via the parametric resonance condition for a given mode number. The results are shown in figure 6. The mean of the extracted parameters from the datasets is $\bar{G} = 4.37$ kPa and $\bar{\mu} = 1.04$ mPa s.

Similarly, we generate noisy data resembling the LIC experiments by solving the full coupled system. We generate 10 datasets varying the maximum radius and maximum stretch ratio as is done experimentally (data not shown). We set the quasi-static shear modulus to $G = 2$ kPa, $\alpha = 2$ and $\mu = 50$ mPa s. Figure 7 shows the histogram counts of calibrated material properties. The mean of the calibrated parameters is accurately determined and $\bar{\alpha} = 2.0$ and $\bar{\mu} = 50.11$ mPa s.

References

[1] Abeid, B.A., Fabiilli, M.L., Aliabouzar, M., Estrada, J.B., 2024. Experimental & numerical investigations of ultra-high-speed dynamics of optically induced droplet cavitation in soft materials. *Journal of the Mechanical Behavior of Biomedical Materials* 160, 106776.

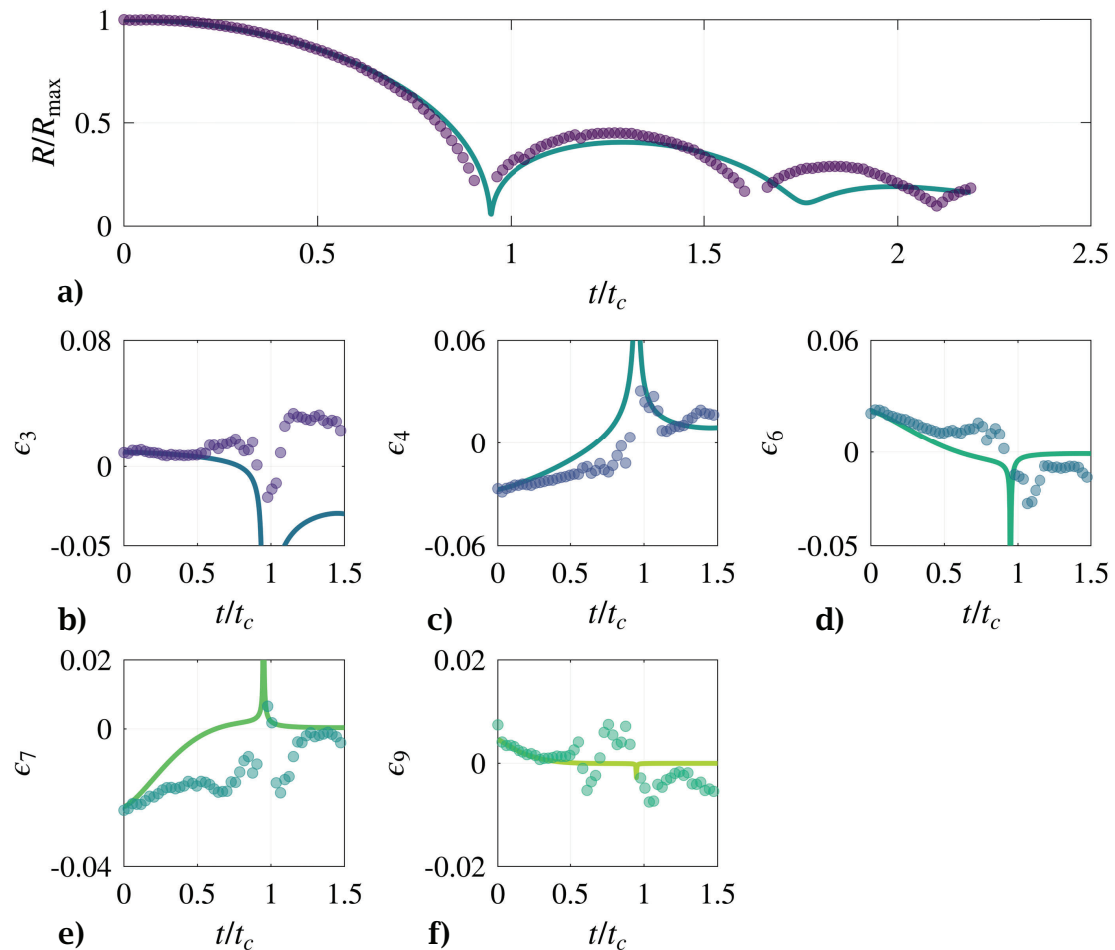


Figure 4: Experiment 2. Non-spherical laser induced bubble **a)** mean radius evolution in time, **b-f)** third, fourth, sixth, seventh, and ninth mode perturbation amplitude over time. Circles: experimental data; and lines: calibrated model prediction.

- [2] Estrada, J.B., Barajas, C., Henann, D.L., Johnsen, E., Franck, C., 2018. High strain-rate soft material characterization via inertial cavitation. *Journal of the Mechanics and Physics of Solids* 112, 291–317.
- [3] Hamaguchi, F., Ando, K., 2015. Linear oscillation of gas bubbles in a viscoelastic material under ultrasound irradiation. *Physics of Fluids* 27, 113103–1–17.
- [4] Kikuchi, H., Keiji Sakai, K.S., Kenshiro Takagi, K.T., 1991. Surface tension wave on gelatin gel. *Japanese Journal of Applied Physics* 30, L1668–1–3.
- [5] Murakami, K., Gaudron, R., Johnsen, E., 2020. Shape stability of a gas bubble in a soft solid. *Ultrasonics Sonochemistry* 67, 105170–1–12.
- [6] Yang, J., Cramer, H.C., Franck, C., 2020. Extracting non-linear viscoelastic material properties from violently-collapsing cavitation bubbles. *Extreme Mechanics Letters* 39, 100839–1–6.
- [7] Yang, J., Tzoumaka, A., Murakami, K., Johnsen, E., Henann, D.L., Franck, C., 2021. Predicting Complex Non-spherical Instability Shapes of Inertial Cavitation Bubbles in Viscoelastic Soft Matter. *Phys. Rev. E* 104, 045108–1–9.
- [8] Yoon, S., Aglyamov, S.R., Karpouk, A.B., Kim, S., Emelianov, S.Y., 2011. Estimation of mechanical properties of a viscoelastic medium using a laser-induced microbubble interrogated by an acoustic radiation force. *The Journal of the Acoustical Society of America* 130, 2241–2248.

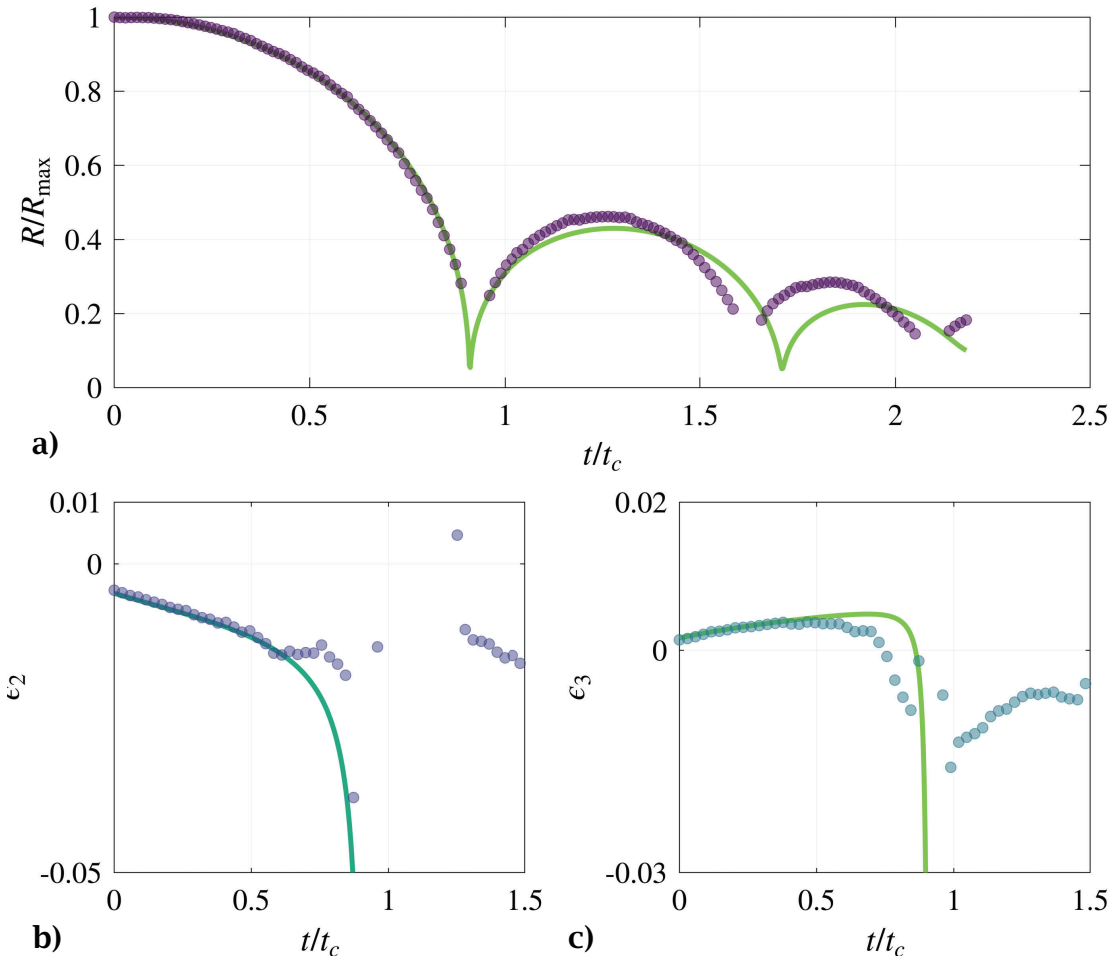


Figure 5: Experiment 3. Non-spherical laser induced bubble **a)** mean radius evolution in time, **b-c)** third, and fourth mode perturbation amplitude over time. Circles: experimental data; and lines: calibrated model prediction.

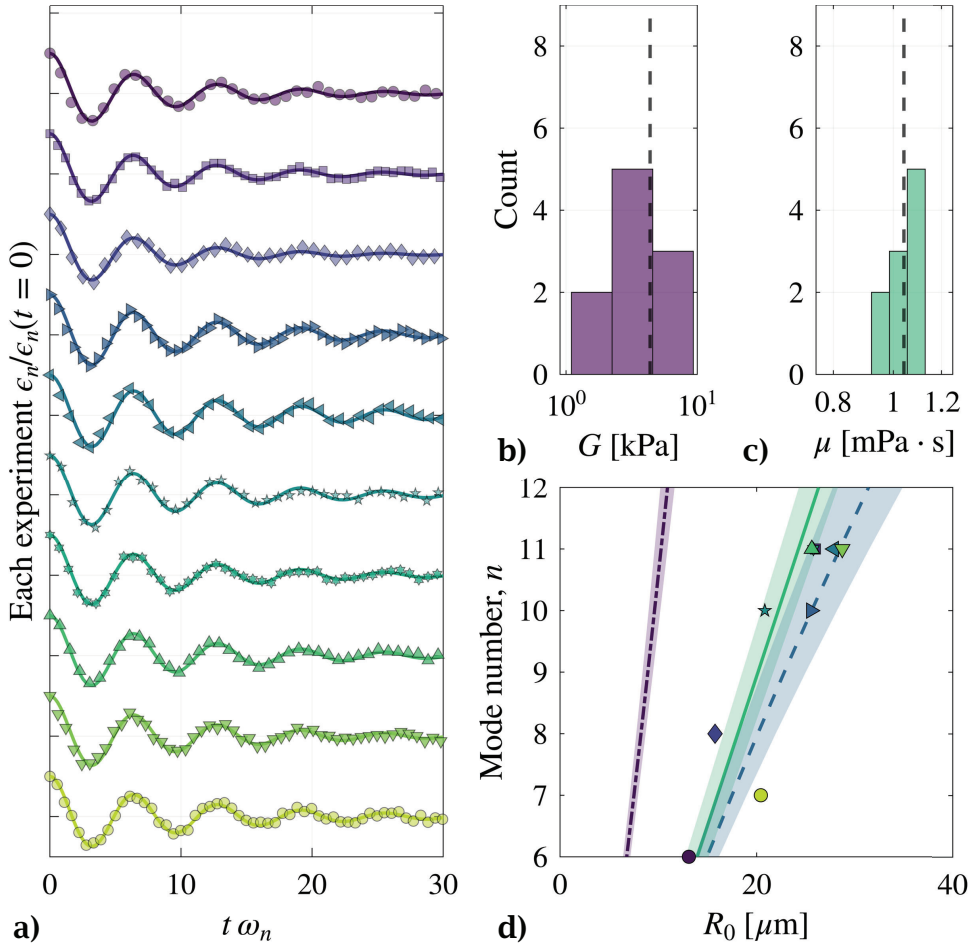


Figure 6: a) Evolution of the normalized amplitude for the most unstable mode for synthetic data, synthetic data (symbols) and model prediction (lines), different colors correspond to different experiments. b) and c) Histograms of the calibrated shear modulus and viscosity, respectively. d) Most unstable mode as a function of equilibrium radius. Green symbols and shaded regions/lines: present synthetic data and current theory, respectively; steel blue: Murakami et al. [5] model; and purple: Yang et al. [7] model. Shaded regions around the mean predictions are from using the standard deviation of the distribution of extracted shear moduli.

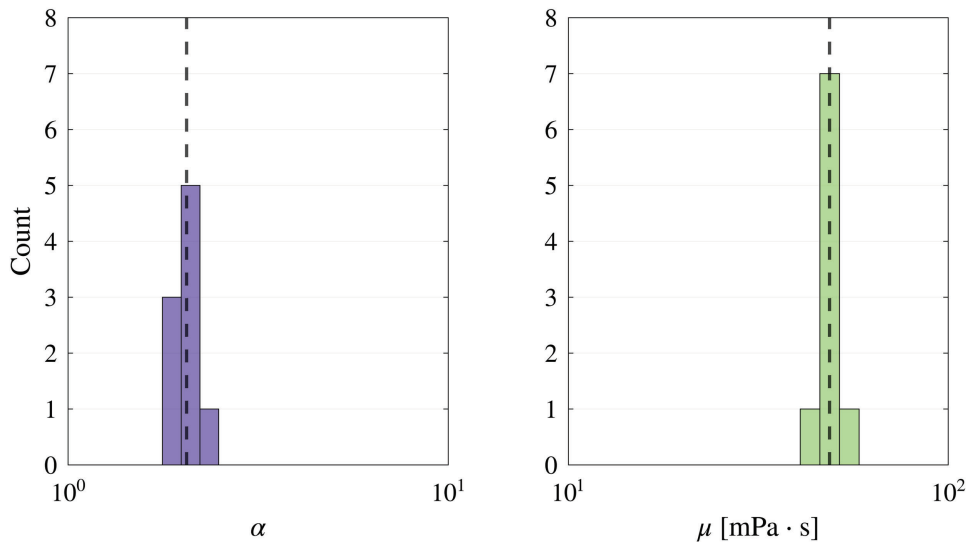


Figure 7: Material property histograms of calibrated parameters from synthetic datasets.